Detailed Dynamic DC Models of VSC Considering Controls for DC-Fault Simulations in Modernized Microgrid Protection

Masoud Davari[®], Senior Member, IEEE, Amir Aghazadeh[®], Weinan Gao, Member, IEEE, and Frede Blaabjerg[®], Fellow, IEEE

Abstract—Nowadays, emerging microgrids have been forming fully integrated power and energy systems using multi-infeed ac/dc (MIACDC) power architectures. An MIACDC power architecture easily integrates renewables, battery energy storage systems, fossil-fuel-based generating units, and various types of loads into one coherent microgrid. Therefore, in modernized microgrids (MMGs), time constants (or equivalently bandwidths) of system dynamics are broad; indeed, multiple controls in different parts of grid-connected voltage-sourced converters (GC-VSCs) create them. For the first time, this article takes into account the detailed dynamics of every GC-VSC's part. It also effectively incorporates their controls to propose "detailed" dynamic dc (DDDC) models for dc-fault simulations. The suggested models are able to simulate dc-fault currents in MMGs' MIACDC power systems more accurately. This research bridges the gap between VSCs' controls and their dynamic dc models, which can be used in dc-fault simulation studies associated with MMG protection. It derives DDDC models of GC-VSCs for two fundamental modes of operation, i.e., P/Q-controlled and V_{DC}/Q -controlled modes. To this end, detailed dynamics of VSCs considering those of ac- and dc-side filters are thoroughly employed using VSCs' space-phasor representation. After linearization, for creating the models mentioned above, relevant GC-VSCs' controls are considered. In order to show the validity of the detailed GC-VSC's dynamic dc models, experimental results are provided. Besides, for studying the models' response to dc faults, adequate comparisons of time-domain simulations of the proposed models and those of the accurate switching models are made. In this regard, an MMG with an MIACDC structure is simulated in PSCAD/EMTDC software; the MMG is implemented first by the proposed VSC's DDDC models and second by the switching ones to generate the simulation results with which one can

Manuscript received April 3, 2020; revised August 4, 2020; accepted October 13, 2020. Date of publication November 6, 2020; date of current version July 30, 2021. This work was supported by the U.S. National Science Foundation (NSF) under Grant #1808279 and Grant #1902787 awarded by the Core Program of Energy, Power, Control, and Networks (EPCN) in the Division of Electrical, Communications and Cyber Systems (ECCS). Recommended for publication by Associate Editor Mahesh S. Illindala. (Corresponding author: Masoud Davari.)

Masoud Davari is with the Department of Electrical and Computer Engineering, Allen E. Paulson College of Engineering and Computing, Georgia Southern University, Statesboro, GA 30460 USA (e-mail: mdavari@georgiasouthern.edu; davari@ualberta.ca).

Amir Aghazadeh is with the School of Electronic and Electrical Engineering, University of Leeds, Leeds LS2 9JT, U.K. (e-mail: elaagh@leeds.ac.uk).

Weinan Gao is with the Department of Mechanical and Civil Engineering, College of Engineering and Science, Florida Institute of Technology (Florida Tech), Melbourne, FL 32901 USA (e-mail: wgao@fit.edu).

Frede Blaabjerg is with the Department of Energy Technology, Aalborg University, 9220 Aalborg, Denmark (e-mail: fbl@et.aau.dk).

Color versions of one or more figures in this article are available at https://doi.org/10.1109/JESTPE.2020.3036409.

Digital Object Identifier 10.1109/JESTPE.2020.3036409

compare. Moreover, in order to reveal the effectiveness of the DDDC models, comparative outputs are produced by simulating conventional models that do not consider dynamics induced by the controllers. Last but not least, comparison outcomes of the DDDC models and those of conventionally adopted models show that this research is able to fill in gaps in the needed models.

Terms—Control structures, dc-fault detailed dynamic dc (DDDC) models, modernized microgrids (MMGs), multi-infeed ac/dc (MIACDC), protection systems, voltage-sourced converters (VSCs).

NOMENCLATURE

$C_{ ext{f-DC}\#k}$	Capacitance of the VSC#k's dc-side filter.
$K_{I_{AC}\#k}(s)$	AC-current controller of the VSC#k's ac side
	in the s domain.
$K_{V_{2,\alpha}\#k}(s)$	DC-voltage controller of the VSC#k's dc side

in the *s* domain.

Inductance of the VSC#k's ac-side filter. $L_{\text{f-AC}\#k}$ $L_{\text{f-DC}\#k}$ Inductance of the VSC#k's dc-side filter. $P_{\text{PCC}\#k}$ Active power injected into the ac-side point of common coupling [positive from the dc side to the ac one (inverter) and negative from the ac side to the dc one (rectifier)].

Reactive power injected into the ac-side point $Q_{\text{PCC}\#k}$ of common coupling (PCC) [positive (reactive power injection) and negative (reactive power absorption)].

Resistance of the VSC#k's ac-side filter. $R_{f-AC\#k}$ Resistance of the VSC#k's dc-side filter. $R_{\text{f-DC}\#k}$ Bandwidth of the VSC#k's most inner current $\omega_{I_{\mathrm{AC}}}$ loop.

Time constant of the VSC#k's ac-side most inner current loop.

 $\vec{i}'_{AC\#k}$ Space-phasor of the current injected to the VSC#k's ac-side filter.

 $\vec{i}_{ ext{AC}\#k}$ Space-phasor of the current injected to the VSC#*k*'s ac-side PCC.

 $\vec{v}_{\text{PCC}\#k}$ Space-phasor of the voltage of the VSC#k's ac-side PCC.

d-component of $\vec{i}_{AC\#k}$. $i_{\text{d-AC}\#k}$ q-component of $\vec{i}_{AC\#k}$. $i_{q-AC\#k}$

Instantaneous power absorbed from the dc *p*Grid-DC#*k* grid #k [positive from the dc side to the ac

one (inverter) and negative from the ac side to

the dc one (rectifier)].

2168-6777 © 2020 IEEE. Personal use is permitted, but republication/redistribution requires IEEE permission. See https://www.ieee.org/publications/rights/index.html for more information.

 $p_{t-AC\#k}$ Instantaneous power injected into the VSC#k's

ac-side boundary.

 $p_{\text{t-DC}\#k}$ Instantaneous power injected into the VSC#k's

dc-side boundary.

 $r_{\text{ON\#}k}$ Resistance of the VSC#k's switch ON-state.

 $i_{DC\#k}$ DC current absorbed from the dc grid #k [positive from the dc side to the ac one (inverter)

and negative from the ac side to the dc one

(rectifier)].

 $i_{dc\#k}$ DC-side current injected to the VSC#k's

dc-side boundary.

 $v_{\text{DC}\#k}$ DC voltage of the VSC#k's dc-side point of

interconnection (dc-grid connection).

 $v_{\text{dc}\#k}$ DC-side voltage of the VSC#k's dc-side

boundary.

 $v_{\text{d-PCC}\#k}$ d-component of $\vec{v}_{\text{PCC}\#k}$. $v_{\text{q-PCC}\#k}$ q-component of $\vec{v}_{\text{PCC}\#k}$.

I. INTRODUCTION

HE emerging power grids have been significantly moving toward simultaneously integrating different power networks and battery energy storage systems into ac/dc grids. They have a multi-infeed ac/dc (MIACDC) architecture in electric power transmission systems (e.g., super grids and meshed high-voltage direct-current power networks) and electric power distribution systems (e.g., hybrid ac/dc microgrids and active distribution systems). All of them are also utilized under the umbrella of smart grids (see [1]–[8] and references therein). Once traditional hybrid ac/dc microgrids are highly applied in serving modernized smart grids, they need to have advanced controls. Those microgrids have been named "modernized microgrids" (MMGs) in this research as they are equipped with sophisticated controls and communications. In smart grids, the MMG concept (which is also based on MIACDC configurations) brings many benefits to the operation, control, and demand-supply within the commercial power systems.

MIACDC-based MMGs will be beneficial to a new trend in power systems' architecture regarded as a fully integrated power and energy system. Fig. 1 shows a concept of an MIACDC-based MMG with a fully integrated power and energy system. An MIACDC-based MMG and its power system have a similar structure to what is employed in traditional power systems. Still, they considerably integrate generating units and power networks, which are configured in dc. This new trend can surely incorporate battery energy storage systems, which are among the presently mature energy storage technologies in the power industry, into traditional power systems. MIACDC-based MMGs require special considerations in the system studies and analyses because their MIACDC power systems significantly utilize a lot of voltagesourced-converter (VSC)-based entities. These devices will bring more flexibility and add features to the MMGs' operations, e.g., augmented energy management, energy arbitrage in the electricity market, improved power quality, and enhanced dynamics using resilient controls.

Consequently, MIACDC-based MMGs necessitate proper deliberations associated with their protection schemes under various conditions. Indeed, because of using a high number of bidirectional VSCs, existing protection schemes need to be revisited. Also, their functionality in the context of new issues and technical scenarios, particularly to the MMGs' MIACDC power systems, must be investigated in detail. For example, one of the promising approaches to the protection of microgrids is adaptive protection schemes. In this regard, many pilot microgrids have used them (see [7] and references therein for the North American ones).

Researchers have conducted a lot of studies on the protection schemes of ac microgrids based on the fault current calculations [7], [9]. In order to have accurate protection schemes in the dc grid of an MMG with the MIACDC structure, we still need to have a precise understanding of what impacts on the dc-side current and analyze them accurately.

There are many detailed ac-side models (e.g., see [10] and references therein)—mostly focusing on ac systems. Notwithstanding, there are limited studies in the field of the VSCs' dc-side models, which are inadequately detailed. As a result, they cause inaccurate simulation results under specific conditions. They have been proposed for both the dc-current and dc-fault calculations (e.g., see [10] and references therein). However, as shown in this article, their results are not accurate enough under some conditions. Indeed, while there are studies in the ac-fault calculations required for the protection schemes of ac microgrids (see [11]–[20]), to the best of our knowledge, research studies lack in detailed dynamic dc (DDDC) models for dc-fault simulations.

Those models are primarily essential when a variety of VSCs is employed in the MIACDC-based architecture of MMGs. It should be pointed out that it is required to investigate DDDC models (considering the detailed dynamics of various components and control aspects of the VSCs) for dc-fault simulations. The reason behind this matter is that the configuration of MMGs results in fully integrated dynamics—including those of VSC's ac and dc sides. Then, DDDC models are required to be accomplished in order to come up with a model incorporating all dynamics, which are affected by the time constants (or equivalently bandwidths) of the closed-loop systems. Those closed-loop dynamics will be interacting with the dc circuit dynamics.

Nevertheless, most studies have only considered the dynamics of the dc-side filter consisting of a dc-side capacitor and inductor (e.g., see [10] and references therein). It means that the impacts of control systems have been overlooked so far, especially when the system gets highly nonlinear (e.g., weak/very-weak-grid integration [21], [22]). These impacts have to be considered since different controls of VSCs (with different topologies) create different time constants, thus affecting the dc fault current accordingly.

Compared with other investigations of dc-voltage dynamics [22]–[24], this research is different, as detailed in the following. Davari *et al.* [23] have proposed a completely different control approach and a different modulation scheme—which is not based on the commonly used PWM—for the "stiff-grid-connected" dc-voltage power ports and not even for P/Q-controlled VSCs. As a result, the model and control introduced in [23] cannot be a correct base for the

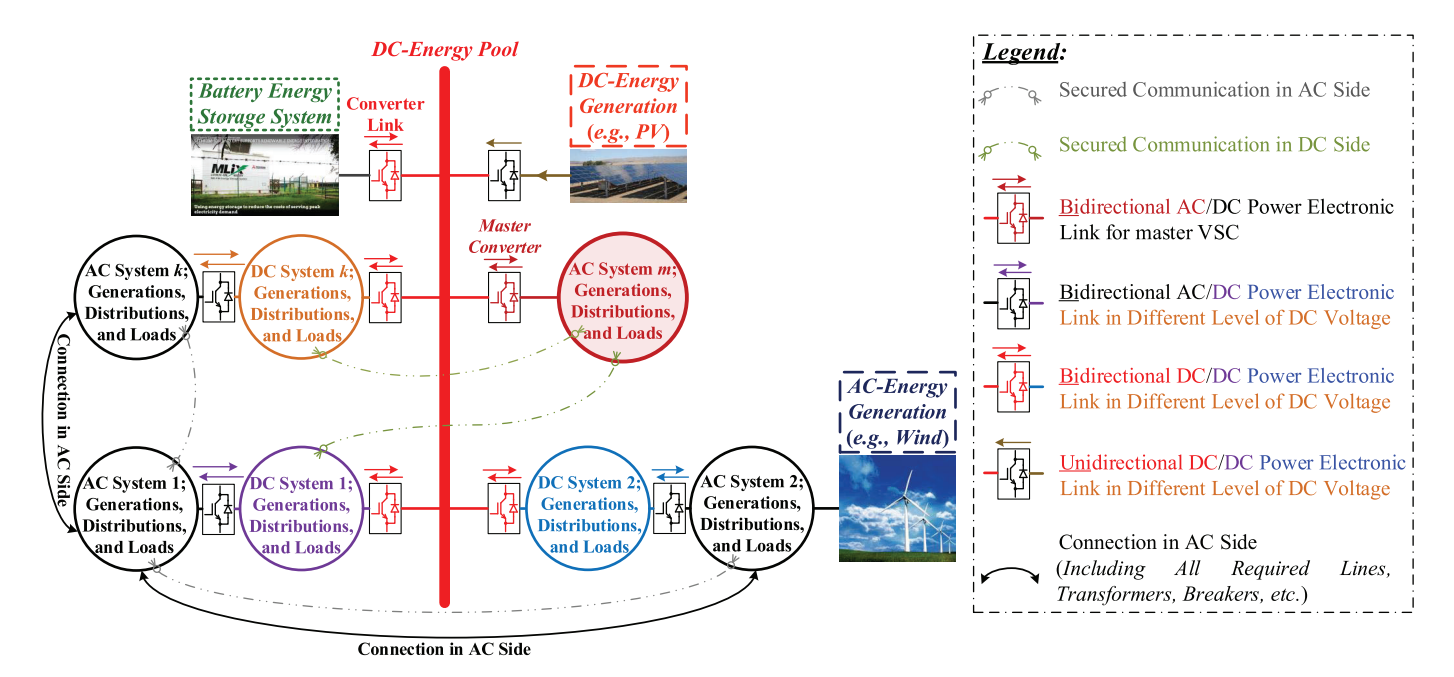


Fig. 1. Concept of the MIACDC-based MMG.

DDDC models proposed for dc-fault simulations in most of the currently running pilot microgrid projects although its methodology yields excellent performance. Besides, Davari and Mohamed [22] have studied the droop coefficient's impacts on the controller response. The industrially accepted, current-controlled, PWM-based VSC was applied in the dc-voltage power port in [22]. It has mainly designed an optimal, robust controller for the stiff-grid-connected dc-voltage power port when changes are being made in the droop coefficient. Thus, the proposed controller has been regulating dc voltage autonomously-and optimally and robustly—via the proposed method. Although it considers the changes in the dynamics due to the variation of both operating points and system parameters, the derived model is somewhat simplified. Again, it has only considered strong grids for the ac power network. Davari and Mohamed [24] have primarily synthesized an optimal, robust controller for the stiff-grid-connected dc-voltage power port based on the industrially accepted, current-controlled, PWM-based VSC. Similar to [22], it has only considered strong grids for the ac power network. Consequently, the dynamic interactions associated with the phase-locked loop (PLL) and grid impedance for designing a controller (just for the dc-voltage power port) have not been seen in [24].

Notably, designing an optimal (e.g., robust, adaptive, and so forth) will be a very challenging task if the model proposed in [22]–[24] is combined with weak-grid-related dynamics. Therefore, as this article's scope is not any control design with specific objectives, this work has adhered to simple, industrially accepted PID controllers for the dc-side/ac-side controllers—in both P/Q-controlled and $V_{\rm DC}/Q$ -controlled VSCs. However, a straightforward application of a PID can only achieve the stabilization of the closed-loop systems. The robustness and optimal response are usually hard to

ensure. For example, just for showing the difficulty and the importance of considering all issues in one single problem, Davari *et al.* [25] have synthesized the controller for the "ac"-side dynamics (not dc-side dynamics) while taking into account all weak-grid-related challenging difficulties. In this regard, the major novelties of this article are as follows.

- Using the VSCs' comprehensive space-phasor representation and some circuit analysis theorems, it thoroughly takes into account the dc-side dynamics, which are affected by both ac and dc sides, to derive a dynamic dc model, which is detailed.
- 2) In addition to considering in-depth dc-side dynamics, it incorporates the control dynamics (ac and dc sides) into the general dynamic dc model to create DDDC models used in the fault calculation of dc grids.
- 3) Considering the above point, this research is able to include and solve the weak-grid-related issues via an effective, yet simple methodology (using some circuit theorems) when deriving with the proposed dynamic dc model. This matter is necessary because problems associated with weak-grid-connected VSCs are complicated as involving with both dynamics of the PLL and those of ac-grid impedance.
- 4) It takes care of two primary modes of VSCs' operation in MMGs with high penetration of power electronic converters. The first one is the fixed active power and reactive power control (i.e., P/Q-controlled VSC), and the second one is the dc-voltage and reactive power control (i.e., V_{DC}/Q -controlled VSC).
- 5) Last but not least, it closes the gap between various controls in the VSCs' ac and dc sides and their dynamic dc models; they can be used in dc-fault simulations and studies associated with the MMGs' protection schemes. The comparison of the results of the proposed

DDDC models with those of conventionally adopted models (which ignore controls and detailed dynamics) reveals that this research fills in gaps in the required models.

Since the models are required to be used in grids with dc faults, experimental examinations should vary as VCSs need to feed faulty networks. Therefore, conducting such tests is almost impossible because of the considerations associated with the safety of devices and personnel. Alternatively, the models have been experimentally assessed here in order to show the validity of the proposed DDDC models.

Finally, in order to demonstrate the validity of the proposed models, this article compares time-domain simulations of an MMG with the MIACDC power system. For comparison, PSCAD/EMTDC software runs it, while all VSCs are implemented using two models. Consequently, one power architecture has been simulated—first, by the proposed VSCs' DDDC models, and second, by their switching models to generate the reference results with which one is able to compare. More importantly, comparative simulation results have also been provided finally. To this end, the conventional models that are only made of and employing dc-side filter parameters (without considering controls) have been simulated. Their results have been compared with the proposed DDDC models' results as well.

The remainder of the article is organized as follows. Section II thoroughly presents DDDC models adopted for various VSCs while incorporating their associated controls. Section II includes experimental results showing the validity of the proposed models. In order to reveal the effectiveness of the proposed models for dc-faults, they should be simulated by PSCAD/EMTDC software, which is one of the appropriate software for accurately simulating different faults in the time domain. In this regard, Section III provides comprehensive simulation results—including comparative simulations. Finally, Section IV concludes the research contributions.

II. DETAILED DYNAMIC DC MODEL ENHANCED BY VSC'S DYNAMICS AND CONTROLS

The VSCs exchange power between an ac grid and a stabilized dc link in MMG's MIACDC power systems. The ac grid's weakness strongly affects the stability and performance of the GC-VSCs (and, hence, those of the overall MIACDC power system). The PLL dynamics interlinked with grid impedance and frequency dynamics cause the instability, mainly provided that the *dq*-frame control is applied [22]. As a result, it is required to embark on investigating the detailed dynamics of various components and control aspects of the VSCs for dc-fault simulations. Full integration of the dynamics—including those of VSC's ac and dc sides—is to be accomplished in order to come up with a model incorporating all dynamics. It is noteworthy that both the control and the VSC topology impact on the dc faults as the time constant of the circuit and that of the closed-loop system is close enough.

Both ac-side and dc-side controls of VSCs under different conditions have been extensively investigated (see [8], [24], and [26]–[32] and references therein). As shown in [24] and [27], the energy stored in the dc-side inductive/capacitive

components and that in the ac-side inductive components of a VSC impact on the VSC's open-/closed-loop dynamics. Therefore, this research takes into account the detailed dc-side dynamics of a VSC in order to be incorporated into the dynamic dc model.

For the power range of microgrids (and also MMGs), the VSCs are the dominant technology in the power electronics industry compared with forced-commutated currentsource converters (CSCs) and so forth [33]. The VSCs to which this article refers should interface different subsystems. That is why they have been referred to as the general term of "VSC"s since their mode of operation is not required to be specified as per the scope of this research. In other words, VSCs may interface a dc subsystem to an ac subsystem with either a unidirectional power flow [21], [25] or a bidirectional one [24]—depending on the required power flow. The full configuration of a grid-connected VSC is shown in Fig. 2. It shows different parts associated with the VSC's energy-storing components and their corresponding power exchange with the ac and dc sides. Without loss of generality, the positive direction of the power is considered to be from the dc side to the ac side. It means that the actual power direction is from the dc side to the ac side. Therefore, the negative power is the rectification mode of operation. A converter is called a rectifier if the flow of average power of $p_{Grid-DC\#k}$ is from the ac side to the dc side, while it is called an inverter if the average power flow of $p_{Grid-DC\#k}$ is from the dc side to the ac side. A similar statement can be discussed for the buck, boost, buck/boost, and more. As a result, the term VSC is kept without loss of generality in this work [33].

One of the most applicable control approaches used in VSCs in MMGs' MIACDC power systems is the current-controlled VSC, by which different parameters are finally controlled through regulating VSC's ac-side currents [7]. The current control is implemented through the most inner loop in the so-called "cascaded" control structure [27]. This article also benefits from the VSC's control structure stated earlier, as it is commonly used because of its salient features [7]. Other articles (e.g., [23], [24], and [27]) have shown that the energy stored in the dc-side inductive/capacitive components and that in the ac-side inductive components of a VSC impact the dynamics, so those dynamics should be considered, as depicted in Fig. 2(b) and (c).

Fig. 2 explains the feasibility of incorporating the closed-loop control dynamics into the generally accepted dynamic model for the dc fault calculations. As discussed in Section I, other researchers have not considered the VSC controls in the required models [as shown in Fig. 2(b) and (c)]. These models have been well proposed in this research since they enable us to incorporate the essential VSC controls into the required models. Besides, with appropriate changes in the inductance and capacitance of the VSC's *LC*-filter on the dc side (e.g., *L*_{f-DC#k} and *C*_{f-DC#k}, respectively), they empower us to include the topology of the VSC in the proposed models.

The key parts in Fig. 2(b) and (c), which are proposed in order to incorporate the dynamics of the ac-side filters and ac-side controller, are $i_{\text{dc}\#k}$ and $v_{\text{dc}\#k}$, respectively. That is why current/voltage sources (which are dependent on the

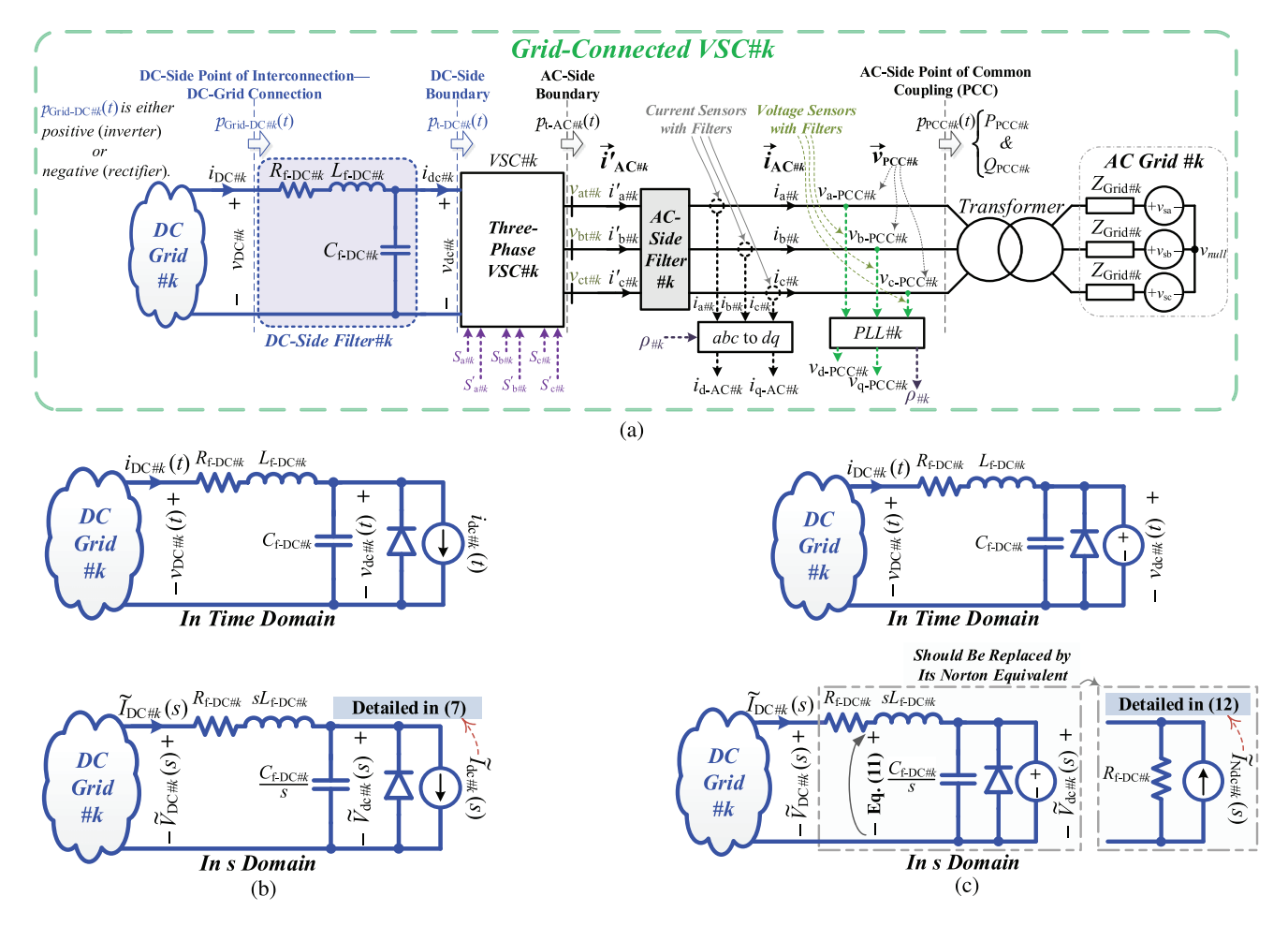


Fig. 2. Grid-connected VSC #k and its DDDC models in an MIACDC structure. (a) Different parameters and parts (including the PLL and so on) of the general grid-connected VSC. (b) DDDC model of the P/Q-controlled VSC #k. (c) DDDC model of the V_{DC}/Q -controlled VSC #k [Eq. (11) is named V'_{dc} #k].

ac-side signals) have been used in order to make the ac-side dynamics connectable to the dc-side ones. In this article, they are selected to transfer the detailed dynamics of the VSC's ac side to the dc side—for which the linearized small-signal dynamic models of VSCs have been considered. Afterward, this article talks about how $i_{\rm dc\#k}$ and $v_{\rm dc\#k}$ are obtained in Fig. 2(b) and (c).

Let us consider an MIACDC power system with a group of \mathcal{M} VSCs; \mathscr{P} denotes the set of VSCs controlled as PQ, and \mathscr{V} represents the set of VSCs controlled as V_{DC}/Q . First, a P/Q-controlled VSC #k (in which $i \in \mathscr{P}$) is considered, and then, V_{DC}/Q -controlled VSC #k (in which $i \in \mathscr{V}$, where $\mathscr{P} + \mathscr{V} = \mathscr{M}$) is taken into account.

A. P/Q-Controlled VSC #k

Since the P/Q-controlled VSC #k controls the active/ reactive power at the PCC, $P_{PCC\#k}/Q_{PCC\#k}$ shown in Fig. 2(a) has to be fixed, and there are other VSCs controlling the dc-side voltage. Therefore, the control output would be $P_{PCC\#k}/Q_{PCC\#k}$, or equivalently i_d/i_q . By means of the instantaneous power balance law across $C_{f-DC\#k}$ and the instantaneous power stored in the "ac"-side filter, referred to Fig. 2(a), one is able to obtain (1), using space-phasor representations

of the three-phase ac-side dynamics [23], [24]. The following equations are able to convey the "detailed" dynamics of such a VSC, whose models are shown in Fig. 2(b).

Now, based on the positive reference power shown in Fig. 2, i.e., from the dc side to the ac side (also known as inverter mode of operation), the following equations are derived in this section. Then, $R_{f-AC\#k}$ represents the resistance of the VSC#k's ac-side filter; $L_{f-AC\#k}$ represents the inductance of the VSC#k's ac-side filter; $r_{ON\#k}$ represents the resistance of the VSC#k's switch ON-state; $\vec{v}_{PCC\#k}$ represents the space-phasor of the voltage of the VSC#k's ac-side PCC; $i_{AC\#k}$ represents the space-phasor of the current injected to the VSC#k's ac-side PCC; $v_{d\text{-PCC\#k}}$ represents the d-component of $\vec{v}_{PCC\#k}$; $v_{q-PCC\#k}$ represents the q-component of $\vec{v}_{PCC\#k}$; $i_{d-AC\#k}$ represents the *d*-component of $\vec{i}_{AC\#k}$; $i_{q-AC\#k}$ represents the q-component of $i_{AC\#k}$; $\omega_{I_{AC}}$ represents the bandwidth of the VSC#k's most inner current loop; $\tau_{I_{AC}}$ represents the time constant of the VSC#k's ac-side most inner current loop; $K_{I_{AC}\#k}(s)$ represents the ac-current controller of the VSC#k's ac side in the s domain; $i_{dc\#k}$ represents the dc-side current injected to the VSC#k's dc-side boundary; $v_{dc#k}$ represents the dc-side voltage of the VSC#k's dc-side boundary; p_{Grid-DC#k} represents the instantaneous power absorbed from the dc grid

#k (positive results in the inverter, and the negative leads to the rectifier mode.); $p_{t\text{-DC}\#k}$ represents the instantaneous power injected into the VSC#k's dc-side boundary; and $p_{t\text{-AC}\#k}$ represents the instantaneous power injected into the VSC#k's ac-side boundary, as listed in the Nomenclature

$$\begin{cases} p_{\text{DC}\#k} = p_{\text{t-AC}\#k} \\ p_{\text{t-AC}\#k} = 1.50L_{\text{f-AC}\#k} \Re \left[\frac{d\vec{i}_{\text{AC}\#k}}{dt} \vec{i}_{\text{AC}\#k}^* \right] \\ + 1.50(R_{\text{f-AC}\#k} + r_{\text{ON}\#k}) \Re \left[\vec{i}_{\text{AC}\#k} \vec{i}_{\text{AC}\#k}^* \right] \\ + 1.50 \Re \left[\vec{v}_{\text{PCC}\#k} \vec{i}_{\text{AC}\#k}^* \right] \end{cases}$$
(1)

where all space-phasor representations have been shown in Fig. 2(a).

Now, using

$$\begin{cases} \Re\left[\frac{d\vec{i}_{\text{AC}\#k}}{dt}\vec{i}_{\text{ac}\#k}^*\right] = 0.5\frac{d}{dt}(i_{\text{d-AC}\#k}^2 + i_{\text{q-AC}\#k}^2) \\ \Re\left[\vec{i}_{\text{AC}\#k}\vec{i}_{\text{AC}\#k}^*\right] = (i_{\text{d-AC}\#k}^2 + i_{\text{q-AC}\#k}^2) \end{cases}$$
(2

one can conclude that

$$p_{\text{t-AC}\#k} = p_{\text{PCC}\#k} + 1.50 \underbrace{\left(R_{\text{f-AC}\#k} + r_{\text{ON}\#k}\right)}_{R_{\text{t-AC}\#k}} \left(i_{\text{d-AC}\#k}^2 + i_{\text{q-AC}\#k}^2\right)$$

$$\text{Conduction Losses Term}$$

$$+ 0.75 L_{\text{f-AC}\#k} \left(\frac{di_{\text{d-AC}\#k}^2}{dt} + \frac{di_{\text{q-AC}\#k}^2}{dt}\right). \quad (3)$$

In (3), the term labeled as "conduction losses term" above (also known as ohmic losses) is associated with the conduction losses (or ohmic ones) of the VSC#k's ac side. It consists of conduction losses of the ac-side filter (i.e., $R_{f-AC\#k}$) and those of the switch ON-state resistance of VSC#k's power electronic switches (i.e., $r_{ON\#k}$). The latter is modeled in the VSC#k's ac side [23], [24], [34], [35]. As a consequence, the newly defined $R_{t-AC\#k}$ considers both $R_{f-AC\#k}$ and $r_{ON\#k}$. Since VSCs have switching losses as well—in addition to conduction losses (modeled by $r_{ON\#k}$ in the ac side)—a term associated with the switching losses is included in the VSC's dc-side boundary. VSC's switching losses are model by either a passive resistive element or an active current source—the term of $(v_{dc\#k}^2/R_{p\#k})$ models the switching losses as the power of static loads, and $P_{Loss\#k}$ is the switching losses of VSC#k if modeled by active components [23], [24], [34], [35]. It is noteworthy provided that passive elements model VSC#k's switching losses (as done by some researchers), and it can be included in $R_{p\#k}$, thus making the mathematics as general as possible. The primary reasoning behind incorporating $R_{p\#k}$ into the model is to take into account any possible ways for modeling switching losses of a converter. They are either a static component, i.e., through an $R_{p\#k}$, or a dynamic element, i.e., via a current source of $I_{\text{Loss}\#k}$ absorbing $P_{\text{Loss}\#k}$, (see [23], [24], [34], and [35] and references therein). As a result, (4) reveals the detailed dynamics of $i_{dc\#k}$ in Fig. 2(a) for the P/Q-controlled

VSCs in MIACDC architectures

$$i_{\text{dc}\#k} = \frac{P_{\text{Loss}\#k}}{v_{\text{dc}\#k}} + \frac{v_{\text{dc}\#k}}{R_{\text{p}\#k}} + \frac{p_{\text{PCC}\#k}}{v_{\text{dc}\#k}} + 1.50 \left(\frac{R_{\text{t-AC}\#k}}{v_{\text{dc}\#k}}\right) i_{\text{d-AC}\#k}^2 + 1.50 \left(\frac{R_{\text{t-AC}\#k}}{v_{\text{dc}\#k}}\right) i_{\text{q-AC}\#k}^2 + 1.50 \left(\frac{L_{\text{f-AC}\#k}}{v_{\text{dc}\#k}}\right) \left(i_{\text{d-AC}\#k}\frac{di_{\text{d-AC}\#k}}{dt}\right) + 1.50 \left(\frac{L_{\text{f-AC}\#k}}{v_{\text{dc}\#k}}\right) \left(i_{\text{q-AC}\#k}\frac{di_{\text{q-AC}\#k}}{dt}\right).$$

$$(4)$$

Finally, as V_{DC} is not the control objective of a P/Q-controlled VSC #k, its nominal value will be employed in linearizing the dynamics around a given operating point (also known as a steady-state operating point). It is noteworthy that (4) is a nonlinear function. Next, one can linearize (4) around the given operating point, which results in

$$\widetilde{i}_{\text{dc}\#k} = \underbrace{\frac{P_{\text{Loss\#k}}}{v_{\text{dc}\#k}}}_{V_{\text{dc}\#k}} + \underbrace{\frac{v_{\text{dc}\#k}}{R_{\text{p\#k}}}}_{R_{\text{p\#k}}}$$
Current Source (Active Element) Current of $R_{\text{p\#k}}$ (Passive Element)
$$+ \underbrace{\frac{1.50 \ I_{\text{d-AC\#k0}}}{V_{\text{DC}0\#k}}}_{V_{\text{DC}0\#k}} \widetilde{v}_{\text{d-PCC\#k}} + \underbrace{\frac{1.50 \ I_{\text{q-AC\#k0}}}{V_{\text{DC}0\#k}}}_{V_{\text{DC}0\#k}} \widetilde{v}_{\text{q-PCC\#k}}$$

$$+ \underbrace{\frac{1.50 V_{\text{PCC\#k0}}}{V_{\text{DC}0\#k}}}_{V_{\text{DC}0\#k}} + \underbrace{\frac{3.00 R_{\text{t-AC\#k}} I_{\text{d-AC\#k0}}}{V_{\text{DC}0\#k}}}_{V_{\text{DC}0\#k}} \widetilde{i}_{\text{d-AC\#k}}$$

$$+ \underbrace{\frac{1.50 L_{\text{f-AC\#k}} I_{\text{q-AC\#k0}}}{V_{\text{DC}0\#k}}}_{V_{\text{DC}0\#k}} \widetilde{i}_{\text{q-AC\#k}}$$

$$+ \underbrace{\frac{3.00 R_{\text{t-AC\#k}} I_{\text{q-AC\#k0}}}{V_{\text{DC}0\#k}}}_{V_{\text{DC}0\#k}} \widetilde{i}_{\text{q-AC\#k}}$$

$$+ \underbrace{\frac{1.50 L_{\text{f-AC\#k}} I_{\text{q-AC\#k0}}}{V_{\text{DC}0\#k}}}_{V_{\text{DC}0\#k}} \widetilde{i}_{\text{q-AC\#k}}$$

$$+ \underbrace{\frac{1.50 L_{\text{f-AC\#k}} I_{\text{q-AC\#k0}}}{V_{\text{DC}0\#k}}}_{V_{\text{DC}0\#k}} \widetilde{i}_{\text{q-AC\#k}}}$$

$$+ \underbrace{\frac{1.50 L_{\text{f-AC\#k}} I_{\text{q-AC\#k0}}}{V_{\text{DC}0\#k}}}}_{D_{\text{co}\#k}} \underbrace{\widetilde{i}_{\text{q-AC\#k}}}_{d_{\text{d}}}$$

$$+ \underbrace{\frac{1.50 L_{\text{f-AC\#k}} I_{\text{q-AC\#k0}}}{V_{\text{DC}0\#k}}}}_{D_{\text{co}\#k}} \underbrace{\widetilde{i}_{\text{q-AC\#k}}}_{d_{\text{d}}}$$

$$+ \underbrace{\frac{1.50 L_{\text{f-AC\#k}} I_{\text{q-AC\#k0}}}}{V_{\text{DC}0\#k}}}}_{D_{\text{co}\#k}} \underbrace{\widetilde{i}_{\text{q-AC\#k}}}_{d_{\text{d}}}$$

$$+ \underbrace{\frac{1.50 L_{\text{f-AC\#k}} I_{\text{q-AC\#k0}}}{V_{\text{DC}0\#k}}}}_{D_{\text{co}\#k}} \underbrace{\widetilde{i}_{\text{q-AC\#k}}}_{d_{\text{d}}}$$

where the superscripts \sim and 0 represent small-signal perturbations and operating point values of the variables, respectively; $v_{d\text{-PCC}\#k}$ and $v_{q\text{-PCC}\#k}$ are the d- and q-components of $\vec{v}_{\text{PCC}\#k}$ as VSC #k is controlled in the dq-frame; and \mathscr{B} and \mathscr{A} defined above are functions of the operating point, as well as parameters, of the ac side of VSC #k. It should be pointed out that (5) can simply be employed in a mathematical linear analysis tool, e.g., \mathscr{L} aplace transform in this article.

Considering Fig. 3(a), if one assumes that the bandwidth of the most inner current loop is $\omega_{I_{AC}}$, the associated time constant will be $\tau_{I_{AC}} = (1/\omega_{I_{AC}})$, which results in the following transfer function from $I_{d\text{-ref}\#k}(s)$ to $I_{d\text{-AC}\#k}(s)$ in the Laplace domain.

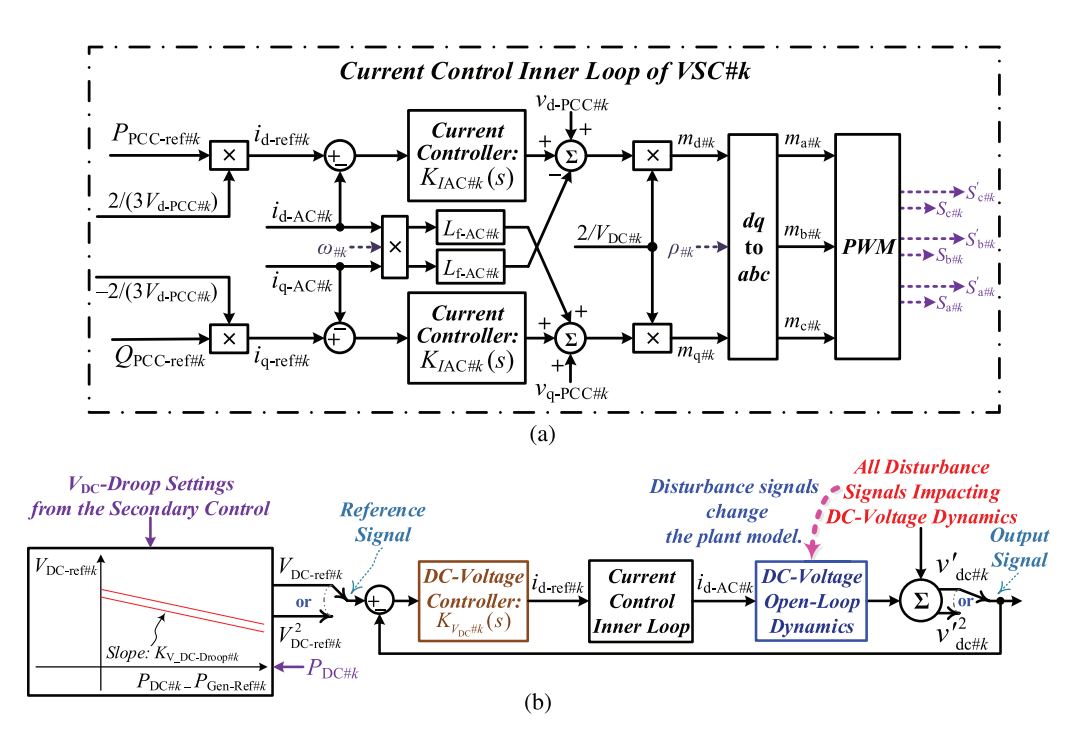


Fig. 3. Two types of common controllers that are employed in the grid-connected VSC #k in Fig. 2. (a) AC-side current controller (i.e., the most inner controller) of the both P/Q- and V_{DC}/Q -controlled VSC #k. (b) DC-voltage controller of the most outer loop of the V_{DC}/Q -controlled VSC #k.

Using
$$\operatorname{TF}_{I_{\operatorname{AC}}\#k}(s) \triangleq (1/(\tau_{I_{\operatorname{AC}}}s+1))$$

$$\begin{cases} \widetilde{I}_{\operatorname{d-AC}\#k}(s) = \operatorname{TF}_{I_{\operatorname{d-AC}}\#k}(s) = \operatorname{TF}_{I_{\operatorname{AC}}\#k}(s) \\ \widetilde{I}_{\operatorname{q-AC}\#k}(s) = \operatorname{TF}_{I_{\operatorname{q-AC}}\#k}(s) = \operatorname{TF}_{I_{\operatorname{AC}}\#k}(s). \end{cases}$$

$$(6)$$

Consequently, using (6), (7) is obtained in the Laplace domain

$$\begin{split} \widetilde{I}_{\text{dc}\#k}(s) &= \underbrace{I_{\text{Loss}\#k}(s)}_{\text{Current Source}} + \underbrace{I_{R_{\text{p}\#k}(s)}}_{\text{Current of Resistor } R_{\text{p}\#k}} \\ &+ \mathscr{A}' \widetilde{V}_{\text{d-PCC}\#k}(s) + \mathscr{A}' \widetilde{V}_{\text{q-PCC}\#k}(s) \\ &+ (\mathscr{A}s + \mathscr{B}) \text{TF}_{I_{\text{AC}}\#k}(s) \widetilde{I}_{\text{d-ref}\#k}(s) \\ &+ (\mathscr{A}''s + \mathscr{B}'') \text{TF}_{I_{\text{AC}}\#k}(s) \widetilde{I}_{\text{q-ref}\#k}(s). \end{split}$$

As a result, (7) is able to incorporate the detailed dynamics of the ac side (including those of the controller and the energy-storing components) into the dynamic model of the P/Q-controlled VSC #k's dc side.

B. V_{DC}/Q -Controlled VSC #k

Since the $V_{\rm DC}/Q$ -controlled VSC #k controls the dc voltage across $C_{\rm f-DC}$ #k and the reactive power at the PCC, the $v_{\rm dc}$ #k/ $Q_{\rm PCC}$ #k shown in Fig. 2(a) is forced to be fixed, and there are other VSCs connected to the dc link (also known as "dc-energy pool" [24]) absorbing/injecting power from/to the dc-side voltage. Thus, the dc-voltage controller outputs the reference signals for the most inner loop controlling i_d/i_q in order to stabilize $V_{\rm DC}/Q_{\rm PCC}$ #k—as current-controlled VSCs are the key enabling technologies in MIACDC power systems. Employing the instantaneous power balance law

across $C_{\text{f-DC\#k}}$ and the instantaneous power stored in the "ac"-side filter, referred to Fig. 2(a), one is able to obtain the following equations by using space-phasor representations of the three-phase ac-side dynamics [23], [24]. As a consequence, the equations below are able to convey the "detailed" dynamics of such a VSC, whose models are shown in Fig. 2(c), where the $i_{\text{dc\#k}}$ direction shows the power transfer from dc side to ac side as the reference.

Again, based on the positive reference power shown in Fig. 2(a), i.e., from the dc side to the ac side (also known as inverter mode of operation), the following equations are derived in this subsection. In addition to the variables defined before (1), $R_{\text{f-DC}\#k}$ represents the resistance of the VSC#k's dc-side filter; $C_{\text{f-DC}\#k}$ represents the capacitance of the VSC#k's dc-side filter; $L_{\text{f-DC}\#k}$ represents the inductance of the VSC#k's dc-side filter; and $K_{V_{\text{DC}}\#k}(s)$ represents the dc-voltage controller of the VSC#k's dc side in the s domain

$$\begin{cases} p_{\text{Grid-DC}\#k} = \frac{v_{\text{dc}\#k}^2}{R_{\text{p\#k}}} + L_{\text{f-DC}\#k} i_{\text{dc}\#k}^2 + p_{C_{\text{f-DC}\#k}} + p_{\text{t-DC}\#k} \\ p_{C_{\text{f-DC}\#k}} = 0.5C_{\text{f-DC}\#k} \frac{dv_{\text{dc}\#k}^2}{dt} = C_{\text{f-DC}\#k} v_{\text{dc}\#k} \frac{dv_{\text{dc}\#k}}{dt} \\ p_{\text{t-DC}\#k} = p_{\text{t-AC}\#k} \end{cases}$$
(8)

where the term of $(v_{\text{dc}\#k}^2/R_{\text{p\#k}})$ models the switching losses as the power of static loads. Also, $P_{\text{Loss\#k}}$ is the switching losses of VSC#k—again, if modeled by active components—and $L_{\text{f-DC\#k}}i_{\text{DC\#k}}^2$ models the instantaneous power stored in $L_{\text{f-DC\#k}}$. It is noteworthy provided that passive elements model VSC#k's switching losses, as done by some researchers (see [23], [34], and [35] and references therein), it can be included in $R_{\text{p\#k}}$, thus making the derived mathematics as

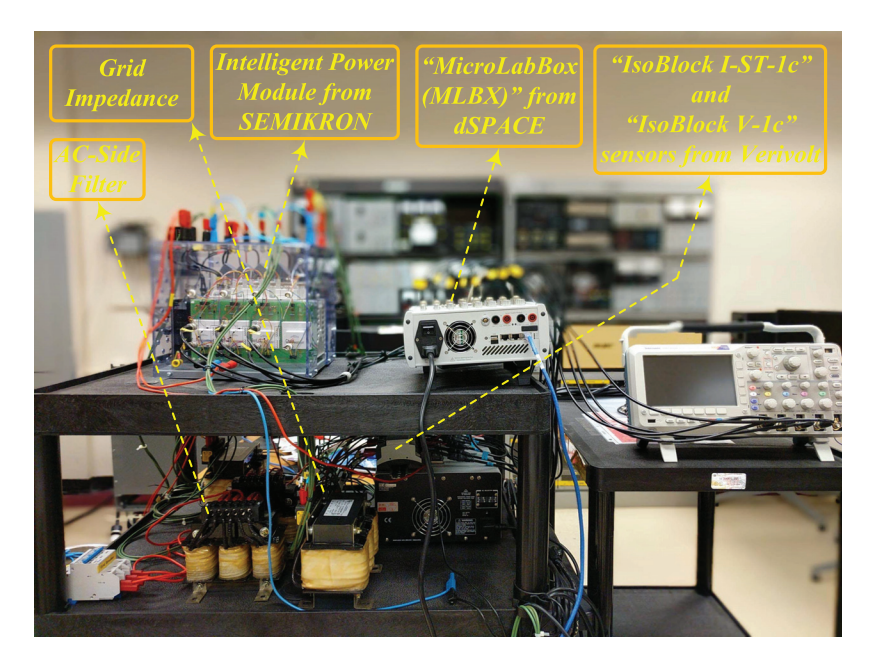


Fig. 4. Test rig used in the experiments.

general as possible. Similarly, the main reason for incorporating $R_{p\#k}$ in the model is to take into account any possible options for modeling converter switching losses, which are either a static element (i.e., via an $R_{D\#k}$) or a dynamic component (i.e., through a current source of $I_{Loss\#k}$ consuming $P_{\text{Loss}\#k}$).

After straightforward mathematical manipulations (similar to the ones mentioned above and also those in [24]), one is able to find (9) from (3)

$$\begin{split} \frac{dv_{\text{dc}\#k}^2}{dt} &= \frac{2}{C_{\text{f-DC}\#k}} \bigg[p_{\text{Grid-DC}\#k} - \frac{v_{\text{dc}\#k}^2}{R_{\text{p}\#k}} - p_{\text{Loss}\#k} - L_{\text{f-DC}\#k} i_{\text{dc}\#k}^2 \\ &- p_{\text{PCC}\#k} - 1.50 R_{\text{t-AC}\#k} i_{\text{d-AC}\#k}^2 \\ &- 1.50 R_{\text{t-AC}\#k} i_{\text{q-AC}\#k}^2 \\ &- 1.50 L_{\text{f-AC}\#k} i_{\text{d-AC}\#k} \frac{di_{\text{d-AC}\#k}}{dt} \\ &- 1.50 L_{\text{f-AC}\#k} i_{\text{q-AC}\#k} \frac{di_{\text{q-AC}\#k}}{dt} \bigg]. \end{split}$$
(9)

Remark 1: It is noteworthy that, in order to reduce the number of nonlinear terms, some researchers take $v_{\text{de}\#k}^2$ as the direct output, so, by controlling $v_{\text{dc#k}}^2$, $v_{\text{dc#k}}$ is "indirectly" controlled [24]. This article, however, discusses $v_{dc\#k}$ control since this research finally needs to have the dynamics of $v_{\mathrm{dc}\#k}$ —not $v_{\mathrm{dc}\#k}^2$.

A $V_{\rm DC}/Q$ -controlled VSC #k controlling the "direct" output of $V_{\rm dc}$ is taken into account here. Equation (9) has described the VSC's nonlinear dynamics in the time domain. It is a dynamic model having the nonlinear terms of $v^2_{\text{dc}\#k}$, $i^2_{\text{d-AC}\#k}$, $i^2_{\text{q-AC}\#k}$, $i_{\text{d-AC}\#k}(di_{\text{d-AC}\#k}/dt)$, and $i_{\text{q-AC}\#k}(di_{\text{q-AC}\#k}/dt)$. Accordingly, one can linearize (9) around a given operating point. Equation (10) demonstrates the linearized transfer function of the nonlinear dynamics of (9) from $V'_{dc\#k}(s)$ to $\widetilde{I}_{d-AC\#k}(s)$, as detailed in [24]; the signal associated with $v'_{\text{dc}\#k}$ has been shown in Fig. 3(b). In order

to adopt this article's variables and notations—and for ease of reference—(10) has expressed the dynamics mentioned above. The coefficients a, b, e, A, B, and E have been described in the Appendix [through (A.1) and (A.2)] using the variables defined in this article

$$\widetilde{V}'_{\text{dc}\#k}(s) = \frac{as^2 + bs + e}{As^2 + Bs + E} \widetilde{I}_{\text{d-AC}\#k}(s) + \text{Disturbance Signals}$$
(10)

where

Disturbance Signal

sturbance Signal
$$\triangleq -\frac{\widetilde{P}_{\text{Grid-DC\#k}}(s)}{As^2 + Bs + E} - \frac{\widetilde{P}_{\text{Loss\#k}}(s)}{As^2 + Bs + E}$$

$$-R_{\text{t-AC\#k}} \frac{\text{Dist}_I(s^2 \widetilde{I}_{\text{q-AC\#k}}(s), s \widetilde{I}_{\text{q-AC\#k}}(s), \widetilde{I}_{\text{q-AC\#k}}(s))}{As^2 + Bs + E}$$

$$-\frac{\text{Dist}_V(\widetilde{V}_{\text{d-PCC\#k}}, \widetilde{V}_{\text{q-PCC\#k}})}{As^2 + Bs + E}.$$

Using (10) and referring to Fig. 3(b), (11) details the resulting closed-loop dynamics

$$\frac{K_{V_{DC}\#k}(s)}{1 + K_{V_{DC}\#k}(s) \frac{as^2 + bs + e}{As^2 + Bs + E}} \times \text{TF}_{I_{AC}\#k}(s)}{1 + K_{V_{DC}\#k}(s) \frac{as^2 + bs + e}{As^2 + Bs + E}} \times \text{TF}_{I_{AC}\#k}(s)} V_{DC\text{-ref}\#k}(s) + \frac{\text{Disturbance Signal Described in (10)}}{1 + K_{V_{DC}\#k}(s) \frac{as^2 + bs + e}{As^2 + Bs + E}} \times \text{TF}_{I_{AC}\#k}(s)}.$$
(11)

Equation (11) is able to incorporate the detailed dynamics of the ac side (including those of the controller and energy-storing components) and those of the dc-side capacitor into the dynamic model of the V_{DC}/Q -controlled VSC #k's dc side. Remarkably, one can replace the capacitor with the model shown in Fig. 2(c), which is based on the "substitution" theorem from the circuit "network theorems" [36]. Based on

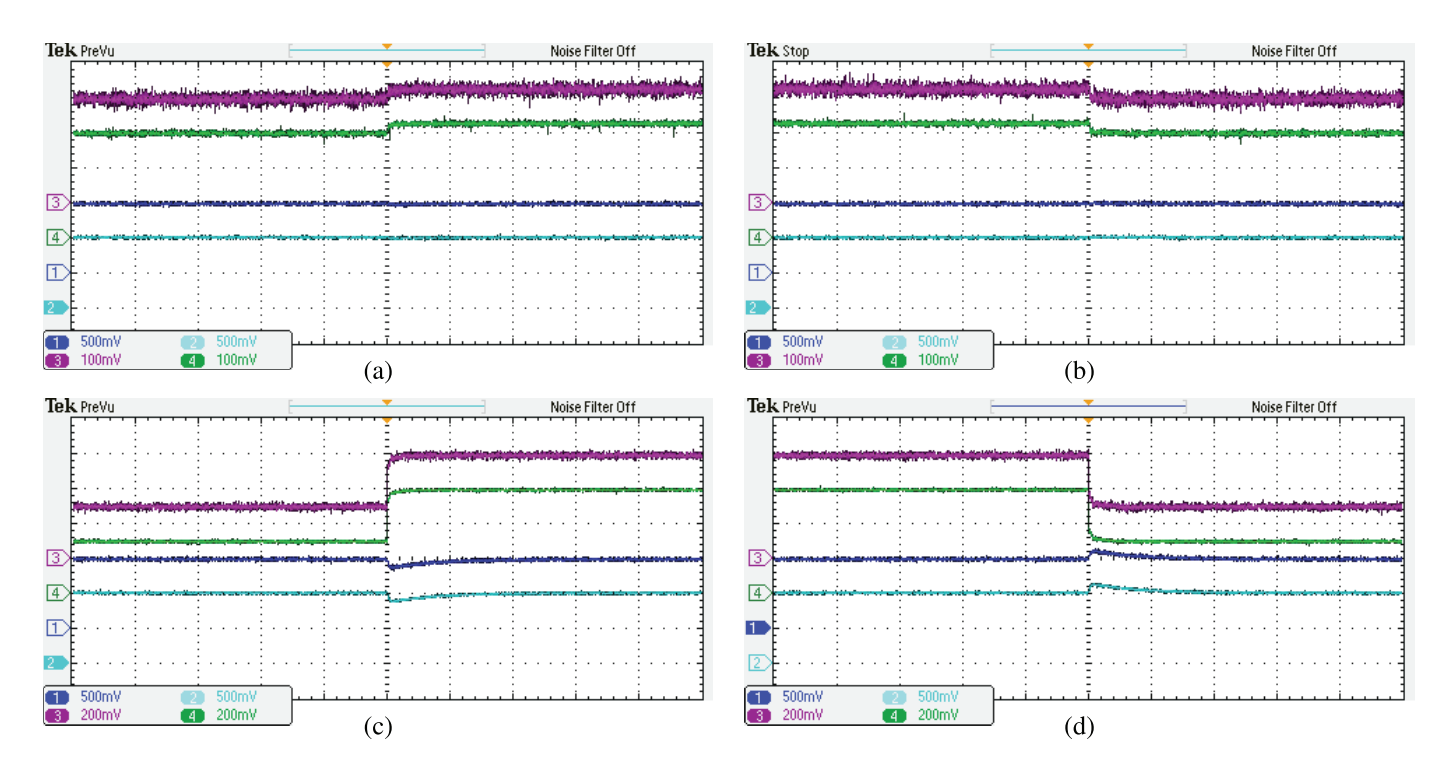


Fig. 5. Model validation of Fig. 2(b) by comparing its results with the response of experimental setup detailed in Fig. 4; horizontal axis: 5 ms/div and vertical axis: v_{DC} (Channel 1 in dark blue for the experiments and Channel 2 in cyan for the model with 200 V/div) and i_{DC} [Channel 3 in dark magenta for the experiments and Channel 4 in lawn green for the model with 2.70 A/div for (a) and (b) and with 5.41 A/div for (c) and (d)]—V/div of each channel has been shown at the left-bottom corner for all variables in per unit (pu).

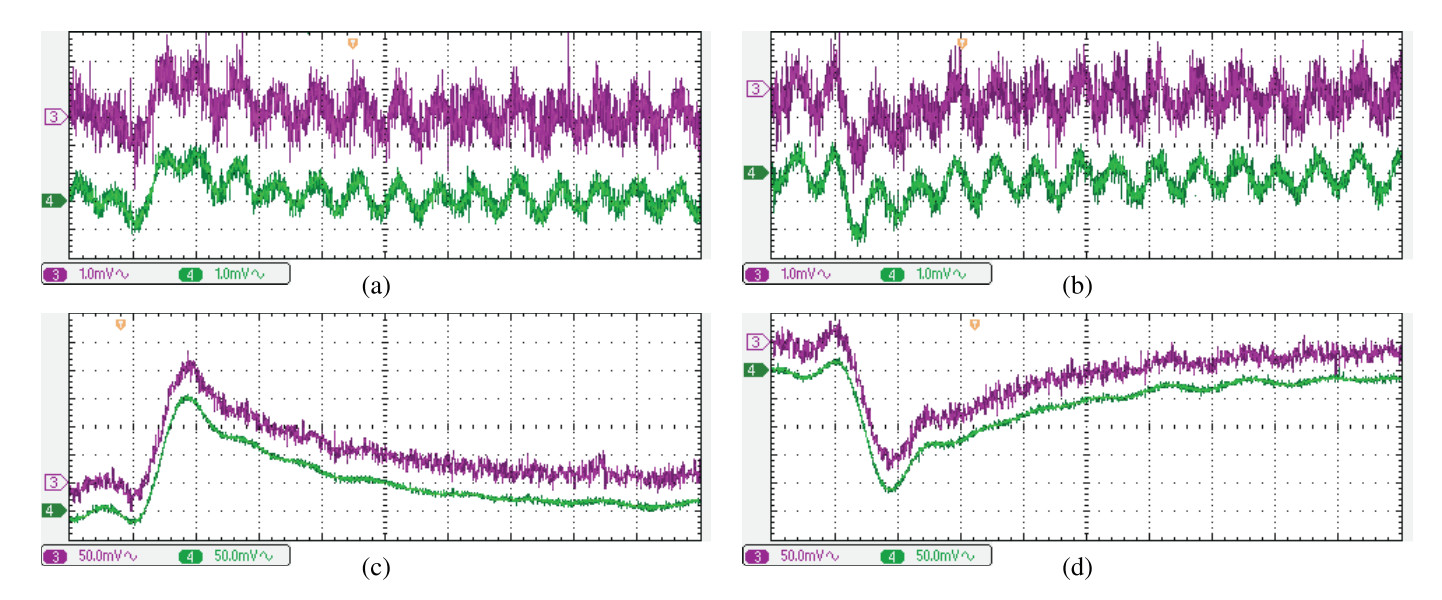


Fig. 6. AC components of different parts of Fig. 5; horizontal axis: 1 ms/div and vertical axis: i_{DC} [Channel 3 in dark magenta for the experiments and Channel 4 in lawn green for the model with 27.03 mA/div for (a) and (b) and with 1.35 A/div for (c) and (d)]—V/div of each channel has been shown at the left-bottom corner for all variables in pu.

Fig. 2(c), finally, one is able to reach the current source model using Norton's theorem, as detailed in the following equation:

$$\begin{split} \widetilde{I}_{\text{Ndc}\#k}(s) \\ &= \frac{K_{V_{\text{DC}}\#k}(s) \frac{as^2 + bs + e}{As^2 + Bs + E} \text{TF}_{I_{\text{AC}}\#k}(s) \times V_{\text{DC-ref}\#k}(s)}{\left[1 + K_{V_{\text{DC}}\#k}(s) \frac{as^2 + bs + e}{As^2 + Bs + E} \times \text{TF}_{I_{\text{AC}}\#k}(s)\right] R_{\text{f-DC}\#k}} \end{split}$$

+
$$\frac{\text{Disturbance Signal Elaborated in (10)}}{\left[1 + K_{V_{DC}\#k}(s) \frac{as^2 + bs + e}{As^2 + Bs + E} \times \text{TF}_{I_{AC}\#k}(s)\right] R_{\text{f-DC}\#k}}$$
. (12)

A previously accomplished load-flow analysis enables us to find the necessary initial values of the state variables. Finally, by using either (7) or (12)—depending on dealing with either P/Q-controlled or $V_{\rm DC}/Q$ -controlled VSC #k—the VSCs' contributions to dc-side fault are simulated by a nodal analysis

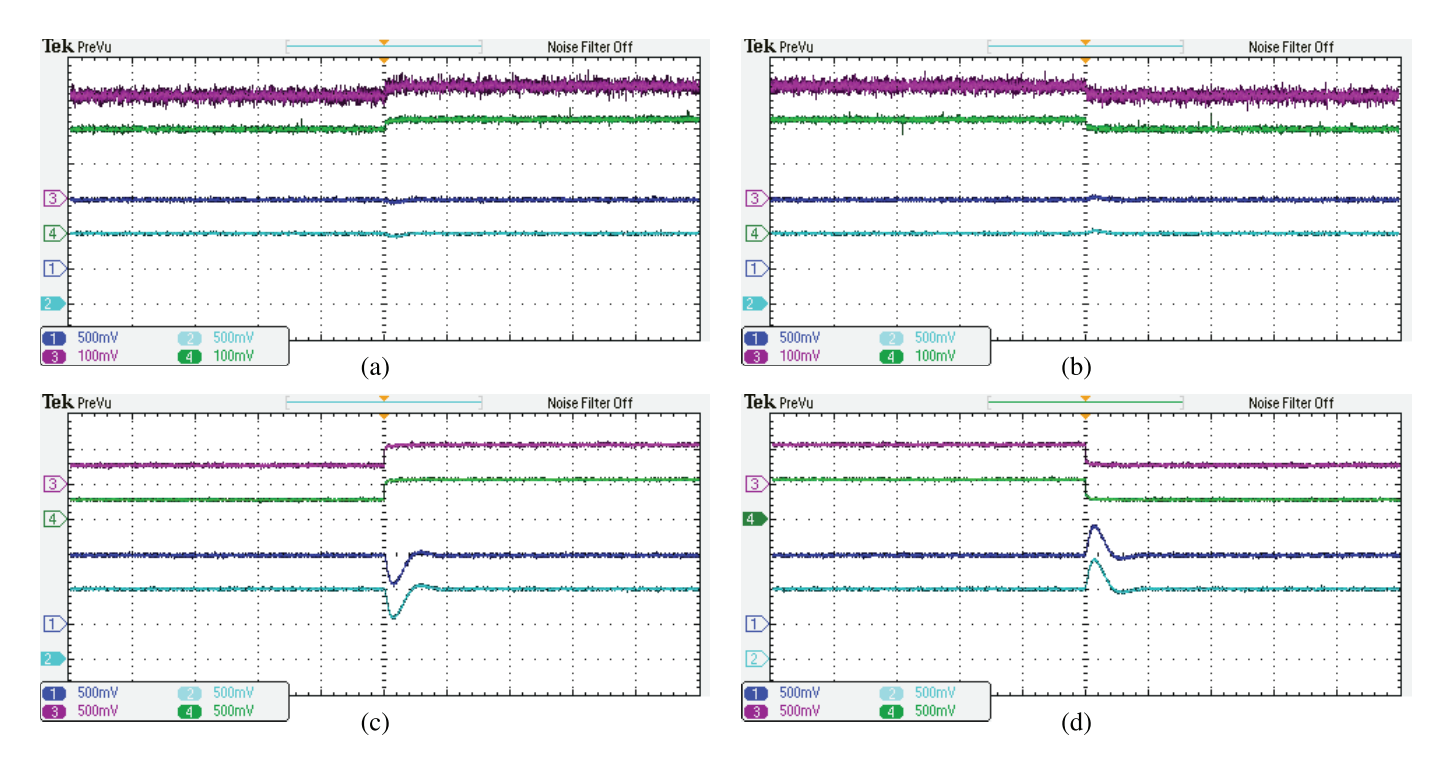


Fig. 7. Model validation of Fig. 2(c) by comparing its results with the response of experimental setup detailed in Fig. 4; horizontal axis: 5 ms/div and vertical axis: v_{DC} (Channel 1 in dark blue for the experiments and Channel 2 in cyan for the model with 200 V/div) and i_{DC} [Channel 3 in dark magenta for the experiments and Channel 4 in lawn green for the model with 2.70 A/div for (a) and (b) and with 13.51 A/div for (c) and (d)]—V/div of each channel has been shown at the left-bottom corner for all variables in pu.

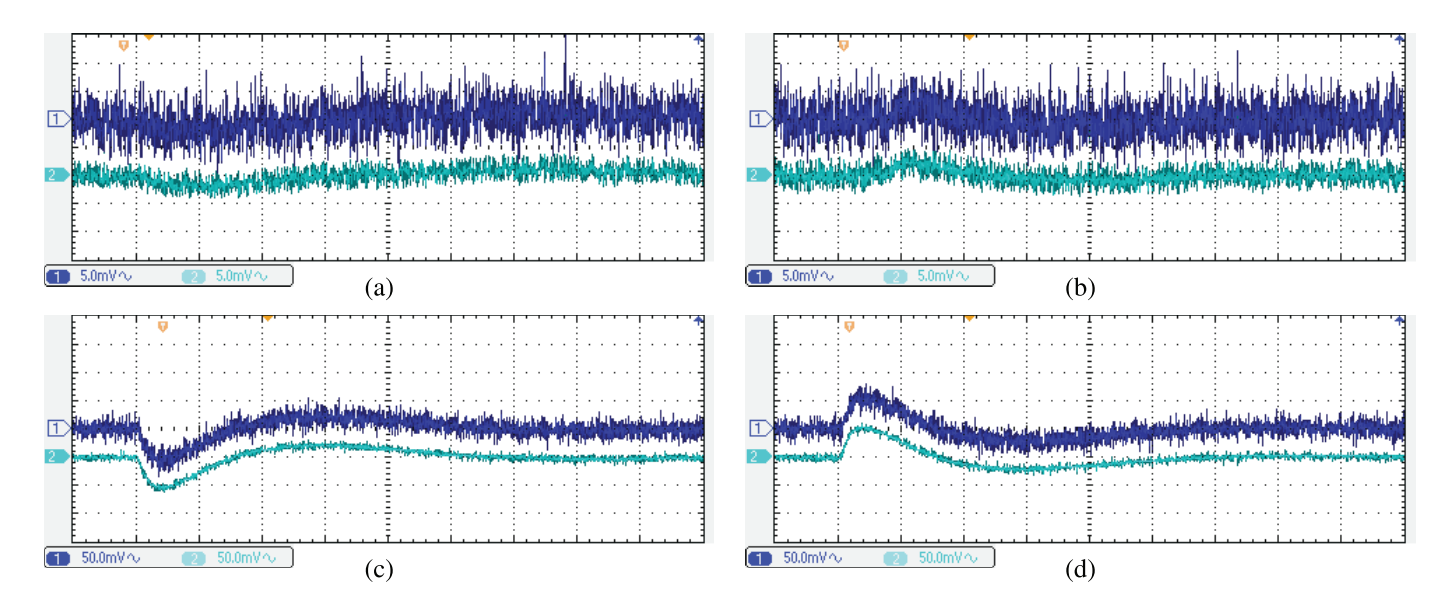


Fig. 8. AC components of different parts of Fig. 7; horizontal axis: 1 ms/div and vertical axis: v_{DC} [Channel 1 in dark blue for the experiments and Channel 2 in cyan for the model with 2.00 V/div for (a) and (b) and with 20 V/div for (c) and (d)]—V/div of each channel has been shown at the left-bottom corner for all variables in pu.

tool; (7) and (12) contain the detailed dynamics of each VSC #k's ac side and incorporate them into the dc side.

C. Model Validations

This section validates the proposed models shown in Fig. 2. They have been validated by comparing their results with the outcomes of the experiments conducted on the VSC demonstrated in Fig. 4. Indeed, the model validation has been

done by comparing the results of the models with those of the prototype of a practical VSC. The main reasons for doing so are that: 1) this validation will be more accurate, as detailed in [21] and 2) it is almost impossible to conduct short-circuit tests on a practical VSC—concerning the safety of devices and personnel. Considering the latter point, this way, it is possible to validate the models using experiments, in addition to the detailed simulations provided in Section III.

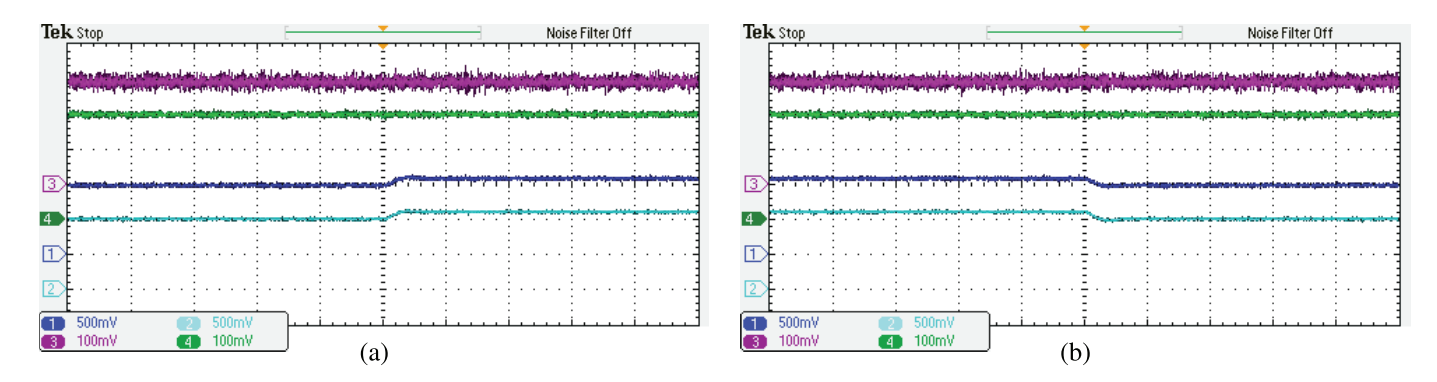


Fig. 9. Model validation of Fig. 2(c) by comparing its results with the response of experimental setup detailed in Fig. 4; horizontal axis: 5 ms/div and vertical axis: v_{DC} (Channel 1 in dark blue for the experiments and Channel 2 in cyan for the model with 200 V/div) and i_{DC} (Channel 3 in dark magenta for the experiments and Channel 4 in lawn green for the model with 2.70 A/div)—V/div of each channel has been shown at the left-bottom corner for all variables in pu.

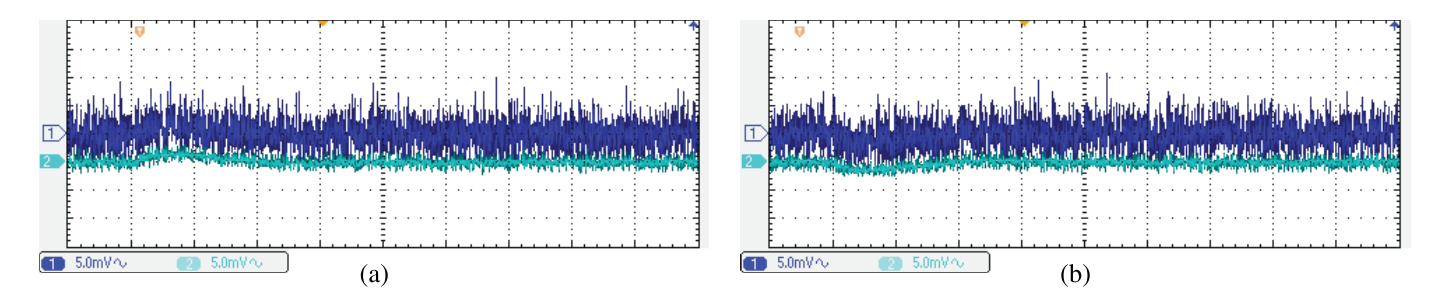


Fig. 10. AC components of different parts of Fig. 9; horizontal axis: 1 ms/div and vertical axis: $v_{\rm DC}$ (Channel 1 in dark blue for the experiments and Channel 2 in cyan for the model with 2.00 V/div)—V/div of each channel has been shown at the left-bottom corner for all variables in pu.

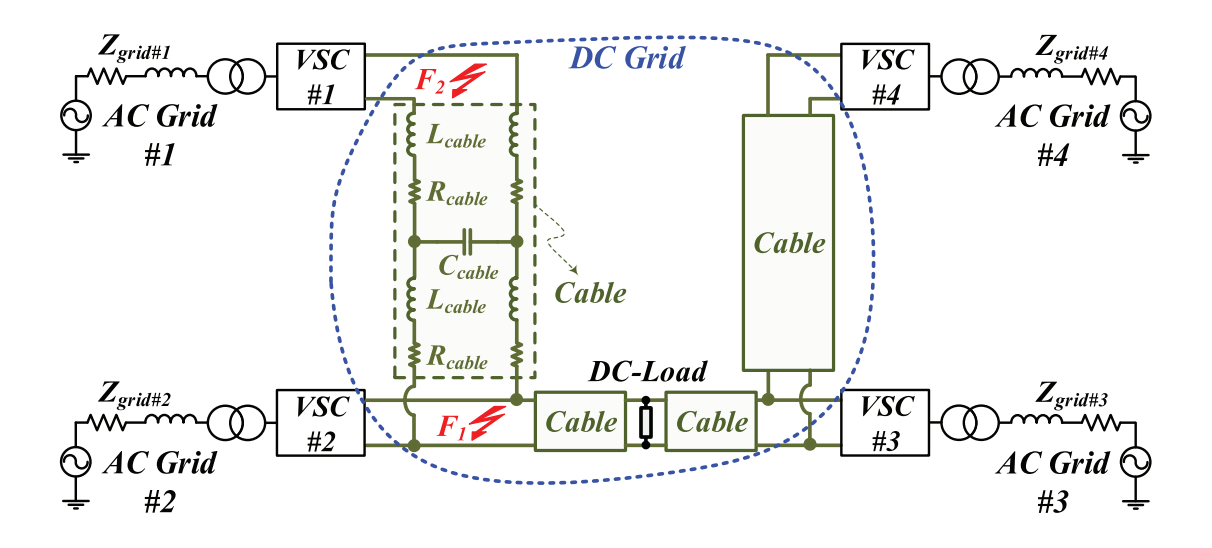


Fig. 11. Combination of VSC #ks in Fig. 2 forming an MIACDC power system.

The results of Fig. 2(a), whose parameters are the same as the experimental setup detailed below, are compared with those of the test rig employed in this article. Fig. 4 has shown the setup, which has the same parameters stated in Table I. The VSI is based on intelligent power modules from SEMI-KRON, including insulated gate bipolar transistors (IGBTs) built by "SKM 50 GB 123 D" modules, "SKHI 22 (AR)" gate drives, and protection circuitry. The dc-link capacitance and

inductance are 2.04 mF and 1.50 mH, respectively. "IsoBlock I-ST-1c" current sensors and "IsoBlock V-1c" voltage sensors from Verivolt Company measure the currents and the voltages, respectively. "MicroLabBox (MLBX)" from dSPACE connects the VSI under test to the measurement's and drive's printed circuit boards (also known as PCBs). In MLBX's architecture, a dual-core, 2-GHz "NXP (Freescale) QorlQ P5020" real-time processor has executed and run the proposed control

TABLE I PARAMETERS OF FIG. 4

Parameter	Value	Parameter	Value
S_n^{-1}	10.81 kVA	SCC ³	35 kVA
L_{f1}/R_{f1}	1.1 mH/0.01 Ω	L_{f2}/R_{f2}	1.1 mH/0.01 Ω
C_f/R_f	15.40 μ F/2.08 Ω	$f_s{}^4$	8.1 kHz
$V_{ m DC}{}^2$	400 V	$V_{ m PCC_{ m Line-to-Line\ rms}}^{ m 2}$	208 V

¹ Nominal VA 3 PCC Short Circuit Capacity Calculating Z_{Grid} [21], [22]

² Nominal Value ⁴ Switching Frequency

algorithm. "Xilinx Kintex-7 XC7K325T" field-programmable gate arrays (also known as FPGAs) have generated the pulsewidth modulation PWM signals connected to digital inputs/outputs (I/Os). The MLBX interface board consists of eight 14-bit, 10 megasamples per second (Ms/s), and differential analog-to-digital channels to interface the measured signals to the controller (with the functionality of free-running mode).

1) Validating the Model of P/Q-Controlled VSC #k: In order to validate the model, Fig. 2(b)—considering (7)—is utilized. When the reference signal inputs are applied to Fig. 2(b), the changes of $V_{\rm dc}$ and $I_{\rm dc}$ are compared with those of the experiments conducted on Fig. 4. For the model verification, different changes (2% and 30%) in power reference signals have been applied, while the VSC's operating point is 0.30 per unit (pu)/0.30 pu for the active/reactive power. For doing so, all the signals and disturbances affecting $V_{\rm dc}$ and $I_{\rm dc}$ in the model have been taken into account while running the model in order to compare the time-domain response of the model with that of the experimental setup.

Fig. 5 depicts the model validation mentioned above. Fig. 5(a) tests a 2% increase in the operating point; Fig. 5(b) examines a 2% decrease in the operating point; Fig. 5(c) assesses a 30% increase in the operating point; and Fig. 5(d) validates a 30% decrease in the operating point. Fig. 6 shows the ac components of the different graphs in Fig. 5. Since the model validation of P/Q-controlled VSC is done here, the ac components of I_{DC} should be investigated as well. For capturing Fig. 6, the oscilloscope has only extracted the "ac" components via removing dc parts to be able to show the graphs on it. Figs. 5 and 6 have demonstrated excellent agreement between the models and the exact switching system.

2) Validating the Model of V_{DC}/Q -Controlled VSC #k: Similarly, in order to validate the model, Fig. 2(c)—considering (12)—is applied. When reference signal inputs are applied to Fig. 2(b), the changes of $V_{\rm dc}$ and $I_{\rm dc}$ are compared with those of the experiments conducted on Fig. 4. For the model verification, different changes (2% and 30%) in power reference signals have been applied, while the VSC's operating point is 0.30 pu/0.30 pu for the active/reactive powers. Also, model validation has tested for a 10% change in the reference signal of the dc voltage. For doing so, all the signals and disturbances affecting $V_{\rm dc}$ and $I_{\rm dc}$ in the model have been considered while running the model in order to compare the time-domain response of the model with that of the experimental setup.

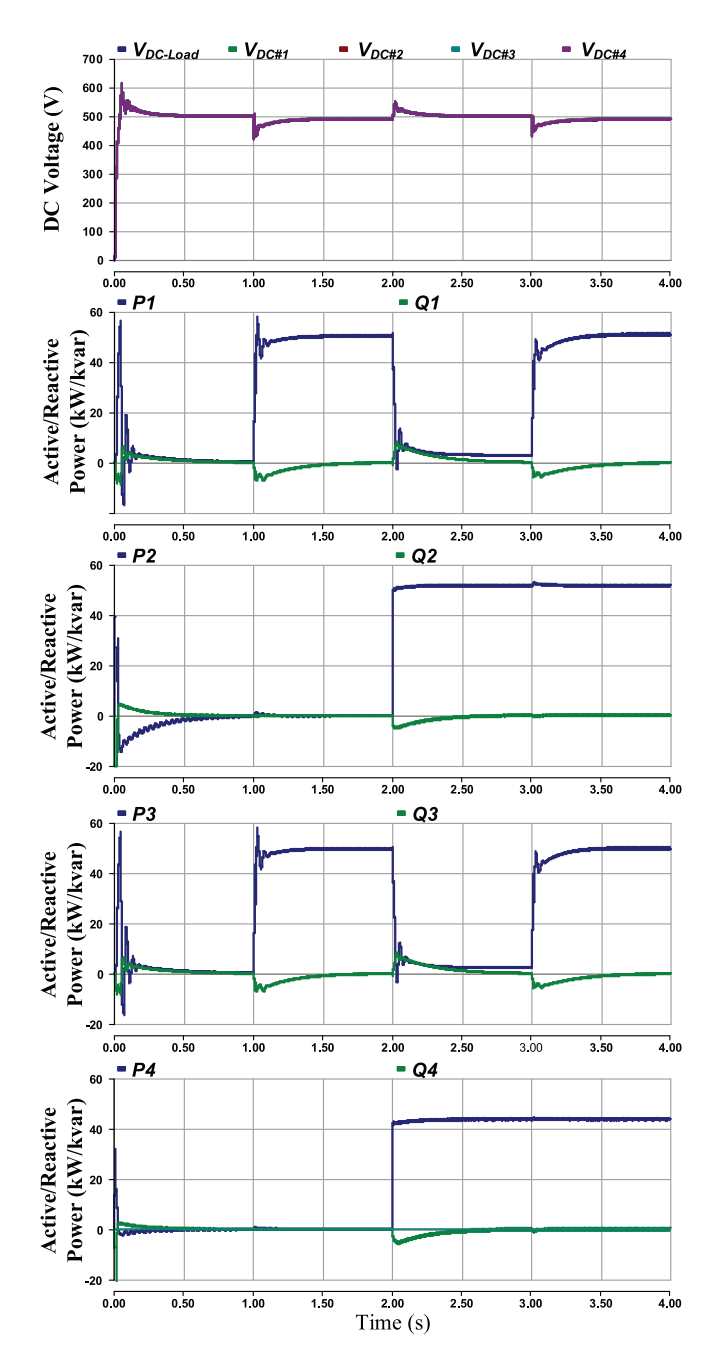


Fig. 12. Normal operation of the system in Fig. 11 showing different VSC's dc voltages and active/reactive powers.

Fig. 7 depicts the model validation mentioned above. Fig. 7(a) tests a 2% increase in the operating point; Fig. 7(b) examines a 2% decrease in the operating point; Fig. 7(c) assesses a 30% increase in the operating point; and Fig. 7(d) validates a 30% decrease in the operating point. Fig. 8 shows the ac components of the different graphs in Fig. 7. Since the model validation of V_{DC}/Q -controlled VSC is done here, the ac components of V_{DC} should be investigated as well. For capturing Fig. 8, the oscilloscope has only extracted the "ac" components via removing dc parts to be able to show the graphs on it. Figs. 7 and 8 have demonstrated excellent agreement between the models and the exact switching system. Moreover, Fig. 9(a) tests a 10% increase in the reference of the dc-voltage operating

Parameter	VSC #1	VSC #2	VSC #3	VSC #4
Control Mode	$V_{ m DC}/Q$	P/Q	$V_{ m DC}/Q$	P/Q
S_n (Nominal Apparent Power) [kVA]	50	50	50	50
$V_{\text{n-AC}}$ (Nominal Low-Side Line-to-Line RMS Voltage) [V]	260	260	260	260
$V_{\text{n-DC}}$ [V]	500	500	500	500
SCCR (for Calculating $Z_{Grid\#k}$ [21], [22])	6.0 & 1.5	6.0 & 1.5	6.0 & 1.5	6.0 & 1.5
f _{Grid} (Grid Frequency) [Hz]	60	60	60	60
f_{swt} (Switching Frequency) [kHz]	8.10	8.10	8.10	8.10
$L_{\text{f-AC\#}k}$ (Inductance of the AC-Side Filter) [mH]	2.40	2.40	2.40	2.40
$R_{\text{t-AC}\#k}$ (Summation of the Resistances $R_{\text{f-AC}\#k}$ and $r_{\text{ON}\#k}$) [Ω]	0.01	0.01	0.01	0.01
$L_{\text{f-DC}\#k}$ (Inductance of the DC-Side Filter) [mH]	2.00	2.00	2.00	2.00
$R_{\text{f-DC}\#k}$ (Resistance of the DC-Side Filter) [Ω]	0.01	0.01	0.01	0.01
Cf.DC#L (Capacitance of the DC-Side Filter) [mF]	6.25	6.25	6.25	6.25

TABLE II

Data of the MIACDC Power System Shown in Fig. 11

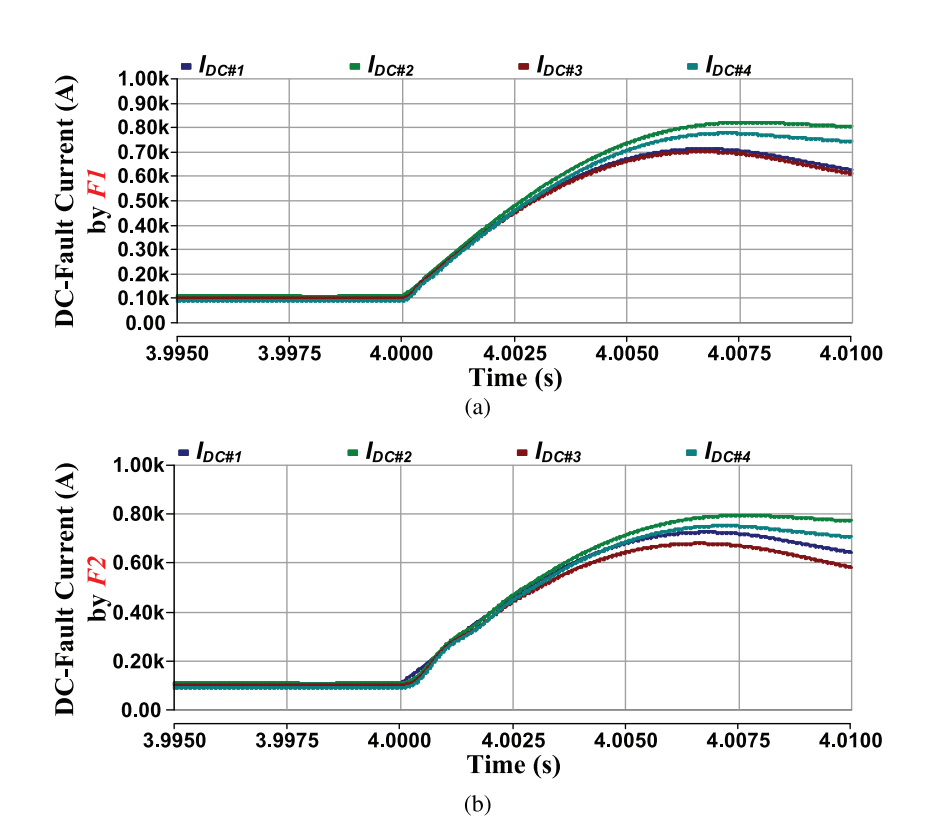


Fig. 13. All VSCs' contributions to the dc faults F_1 and F_2 illustrated in Fig. 11 (presentation's time window: 10 ms). (a) DC-current contributions caused by fault F_1 . (b) DC-current contributions caused by fault F_2 .

point, and Fig. 9(b) examines a 10% decrease in the reference of the dc-voltage operating point. Again, Fig. 10 has demonstrated the ac components of Fig. 9. Figs. 7 and 8 have also displayed excellent agreement between the models and the exact switching system.

III. SIMULATION RESULTS

This section details the simulations of the proposed models and compares their simulation results with the outcomes of the VSCs' actual switching models. PSCAD/EMTDC software is one of the tools that are frequently being employed in

simulating the switching model of VSCs with high accuracy. Therefore, for simulation purposes, an MIACDC-based MMG (as depicted in Fig. 11) has been modeled and run in PSCAD/EMTDC software. Table II provides the parameters of Fig. 11, which includes all the modes discussed above, in order to evaluate the grid's performance in both normal and short-circuit conditions. While two VSCs (named VSC #1 and VSC #3) are $V_{\rm DC}/Q$ -controlled, VSC #2 and VSC #4 are P/Q-controlled VSCs injecting constant power. The nominal power of all VSCs is 50 kVA. In addition, the resistance, inductance, and capacitance of the cable used to connect those VSCs are 0.82 m $\Omega/{\rm km}$, 0.98 $\mu{\rm H/km}$, and 0.014 $\mu{\rm F/km}$,

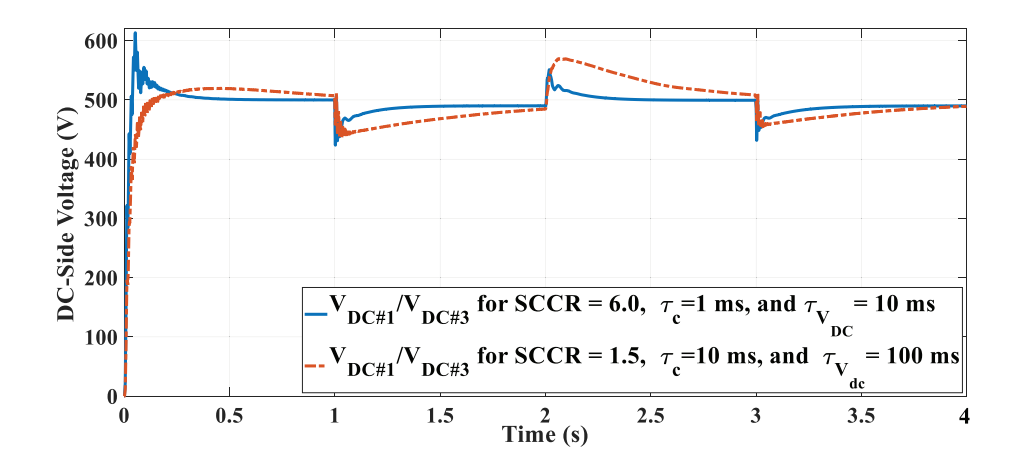


Fig. 14. DC voltage of VSC #1/VSC #3 for SCCR = 6 and $\tau_{VDC} = 10$ ms, as well as SCCR = 1.5 and $\tau_{VDC} = 100$ ms.

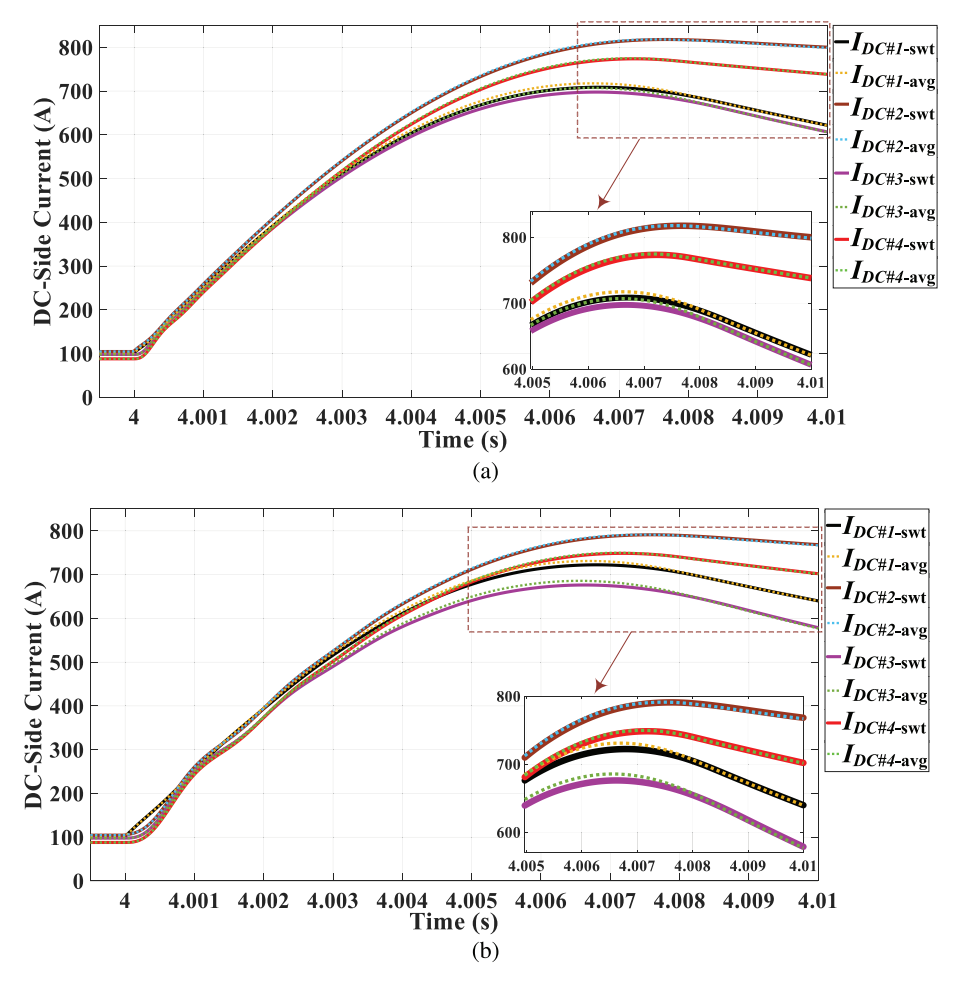


Fig. 15. All VSCs' contributions to faults F_1 and F_2 using switching and DDDC models of VSCs #1–#4; the former is indicated dy "-swt," and the latter is denoted by "-avg"—for SCCR = 6, $\tau_{I_{AC}} = 1$ ms, and $\tau_{V_{DC}} = 10$ ms (presentation's time window: 10 ms). (a) Results of dc fault F_1 . (b) Results of dc fault F_2 .

respectively. Also, "Pi" models of the lines have been considered. Furthermore, the VSCs' parameters have been tabulated in Table II. The dc grid of the abovementioned microgrid supplies two 100-kW dc loads, which have been connected to the dc power network at t=1 s and t=3 s, respectively, in the simulation.

Fig. 11 is examined for different grid impedances considering the short-circuit capacity ratio (SCCR) defined in [22]. To evaluate the normal performance of the MMG, it is tested under SCCR = 6 and dc-voltage/current controllers of $K_{V_{\rm DC}\#k}(s)/K_{I_{\rm AC}\#k}(s)$ resulting in the time constants of $\tau_{I_{\rm ac}}=1$ ms for all current control loops and $\tau_{V_{\rm dc}}=10$ ms for

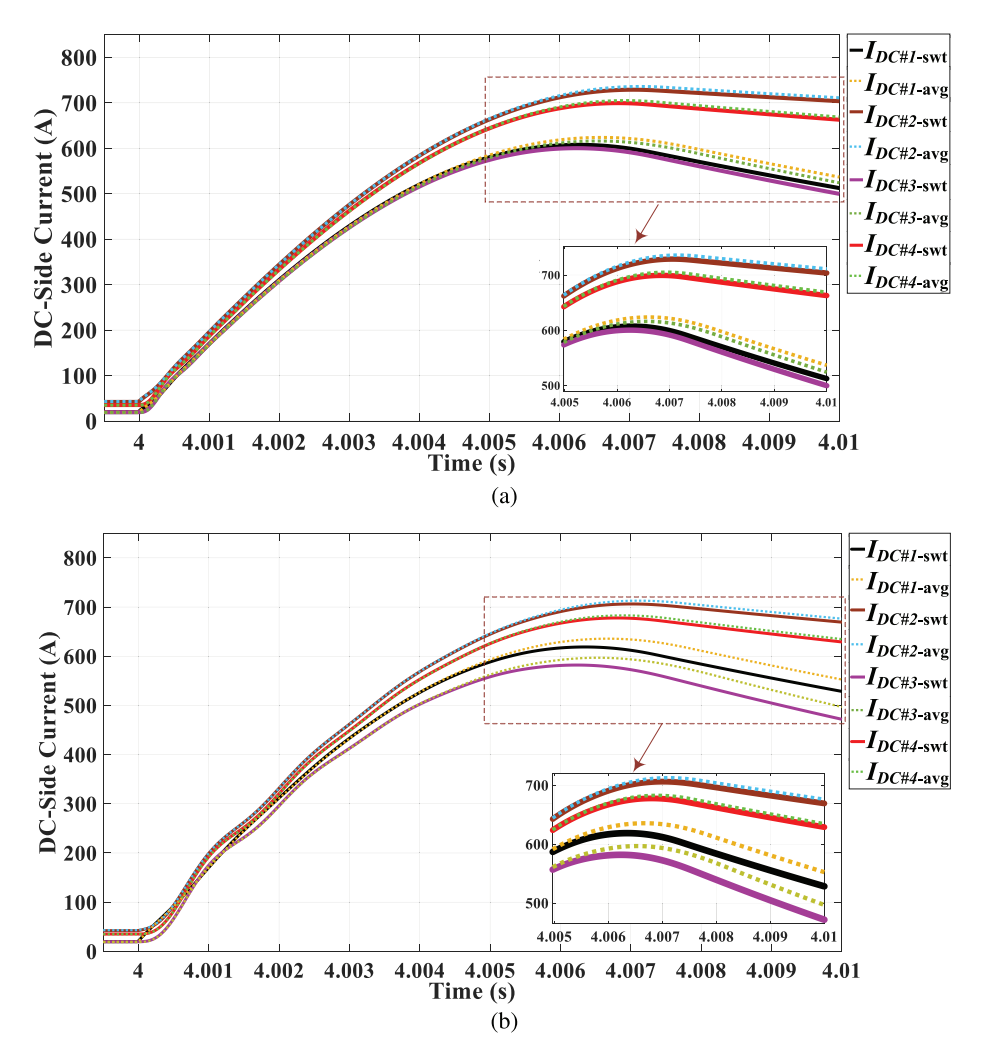


Fig. 16. All VSCs' contributions to faults F_1 and F_2 using switching and DDDC models of VSCs #1–#4; the former is indicated by "-swt," and the latter is denoted by "-avg"—for SCCR = 1.5, $\tau_{I_{AC}} = 10$ ms, and $\tau_{V_{DC}} = 100$ ms (presentation's time window: 10 ms). (a) Results of dc fault F_1 . (b) Results of dc fault F_2 .

all dc-voltage loops. Different VSCs' dc voltage and active/reactive power have been depicted in Fig. 12. It shows that the dc voltage is adjusted to 500 V by VSC #1 and VSC #3. At t = 1 s, when the first dc load—which is 100 kW—is connected to the dc-side of the microgrid, these two VSCs need to provide the dc power demand and control the dc voltage. The amount of active power generated by VSC #1 is shown in Fig. 12. Based on this figure, VSC #1 injects 50 kW at t = 1 s in order to adjust the dc voltage. At t = 2 s, when both P/Q-controlled inverters start injecting active power to the grid, VSC #1 and VSC #3 adjust their power to regulate the dc voltage. Again at t = 3 s, the second 100 kW dc load is connected to the dc grid. At this time, similar to t = 1 s, VSC #1 and VSC #3 generate the active power demanded in order to control the dc voltage. Eventually, two separate 10-ms faults (i.e., F_1 and F_2 shown in Fig. 11) occur at t = 4.0 s; all VSCs' contributions to F_1 and F_2 have been demonstrated in Fig. 13(a) and (b), respectively.

A. Proposed Models—Which Are Considering Detailed Dynamics With Controllers

Here, for validating the models proposed in Fig. 2(b) and (c), the performance of the system using various $K_{V_{DC}\#k}(s)/K_{I_{AC}\#k}(s)$ (resulting in different time constants of $\tau_{I_{ac}}$ for all current control loops and $\tau_{V_{DC}}$ for all dc-voltage control loops) has been investigated and evaluated. In this regard, the dc voltage of VSC #1 for the cases of SCCR = 6 and $\tau_{V_{DC}}$ = 10 ms, as well as SCCR = 1.5 and $\tau_{V_{DC}}$ = 100 ms, has been depicted in Fig. 14. It is noteworthy that, in Fig. 14 (and also in Figs. 15 and 16), PSCAD software has generated the data, but they have depicted by MATLAB. According to Fig. 14, it is clear that, for both conditions, $K_{V_{DC}\#k}(s)/K_{I_{AC}\#k}(s)$ controls dc voltage and current (in the dq-frame) with different time constants (or equivalently the bandwidth induced by the controller) appropriately.

In order to examine the proposed models, the MIACDC power system (depicted in Fig. 11) is simulated by employing switching models of VSCs and their pertinent models proposed

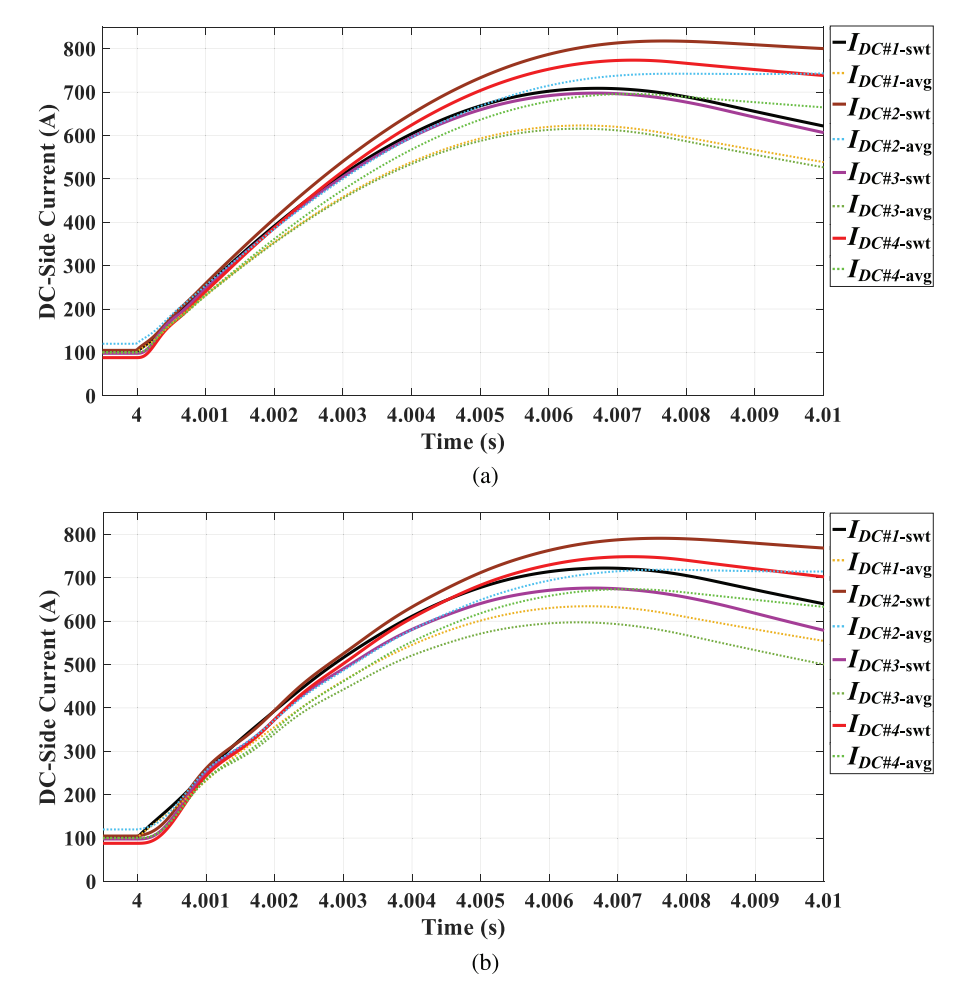


Fig. 17. Simulations of Fig. 15 for the dynamic dc model of the P/Q-controlled VSC #k and the V_{DC}/Q -controlled VSC #k—without considering $TF_{I_{AC}\#k}(s)$ and $K_{V_{DC}\#k}(s)/K_{I_{AC}\#k}(s)$ —subparts are not required to be shown here because the difference between the results of the switching models and those of the employed models is transparent and legible.

in Fig. 2(b) and (c). In other words, the performance of two MIACDC power systems—one with only switching models of VSCs and another one with solely DDDC models of VSCs—is compared. For both MMGs, two 10-ms faults occur at t=4.0 s, which are F_1 and F_2 (referred to Fig. 11). Thereinafter, the results of the MIACDC power system with all the accurate switching models of VSCs use subscripts ending with "-swt." Besides, those of the MIACDC power systems with all the proposed models employ subscripts ending with "-avg."

The first test case for dc-fault current simulation is done on the MIACDC system with SCCR = 6 (i.e., strong ac grid [22]) and $\tau_{I_{AC}}$ = 1 ms and $\tau_{V_{DC}}$ = 10 ms. In this case, the total dc loads are 200 kW, i.e., two 100-kW dc loads, and they are connected to the microgrids at t=1 s and t=3 s in the simulation, respectively. $K_{V_{DC}\#k}(s)/K_{I_{AC}\#k}(s)$ results in the time constants of $\tau_{I_{AC}}$ = 1 ms for all current control loops and $\tau_{V_{DC}}$ = 10 ms for all dc-voltage loops. The fault current contributions of all VSCs for the MIACDC power network have been shown in Fig. 15. It reveals that for, F_1 's and F_2 's locations [see Fig. 15(a) and (b)], the MIACDC power system in which all dynamic models are utilized is able to respond to dc-faults similar

to the MIACDC power system implemented by all switching models of VSCs. This observation is valid not only for current transients but also for the steady-state of the currents in the system.

The second test case for dc-fault current simulation is conducted on the MIACDC system with SCCR = 1.50 (i.e., very weak ac grid [22]), $\tau_{I_{AC}} = 10$ ms, and $\tau_{V_{DC}} = 100$ ms, which is selected to investigate the performance of the DDDC models proposed. Because of dealing with a weaker grid condition, typically, the amount of active power will decrease. In this test scenario, the total amount of load is selected to be a 60-kW dc load, including two 30-kW dc loads. Two PQ-Controlled VSCs inject 40 kW at t = 2 s, which results in a change in the VSC #1's/VSC #3's mode of operation. This case is able to excite nonlinear dynamics because of having very weak grids, in addition to variations in the mode of operation. All VSCs' dc-current contributions to the dc faults of F_1 and F_2 —for both DDDC-model- and switching-modelbased MIACDC grid—have been demonstrated in Fig. 16. Fig. 16(a) for F_1 and Fig. 16(b) for F_2 show close agreement between the time-domain simulation of the switching models and that of the proposed models as all results match with their counterparts.

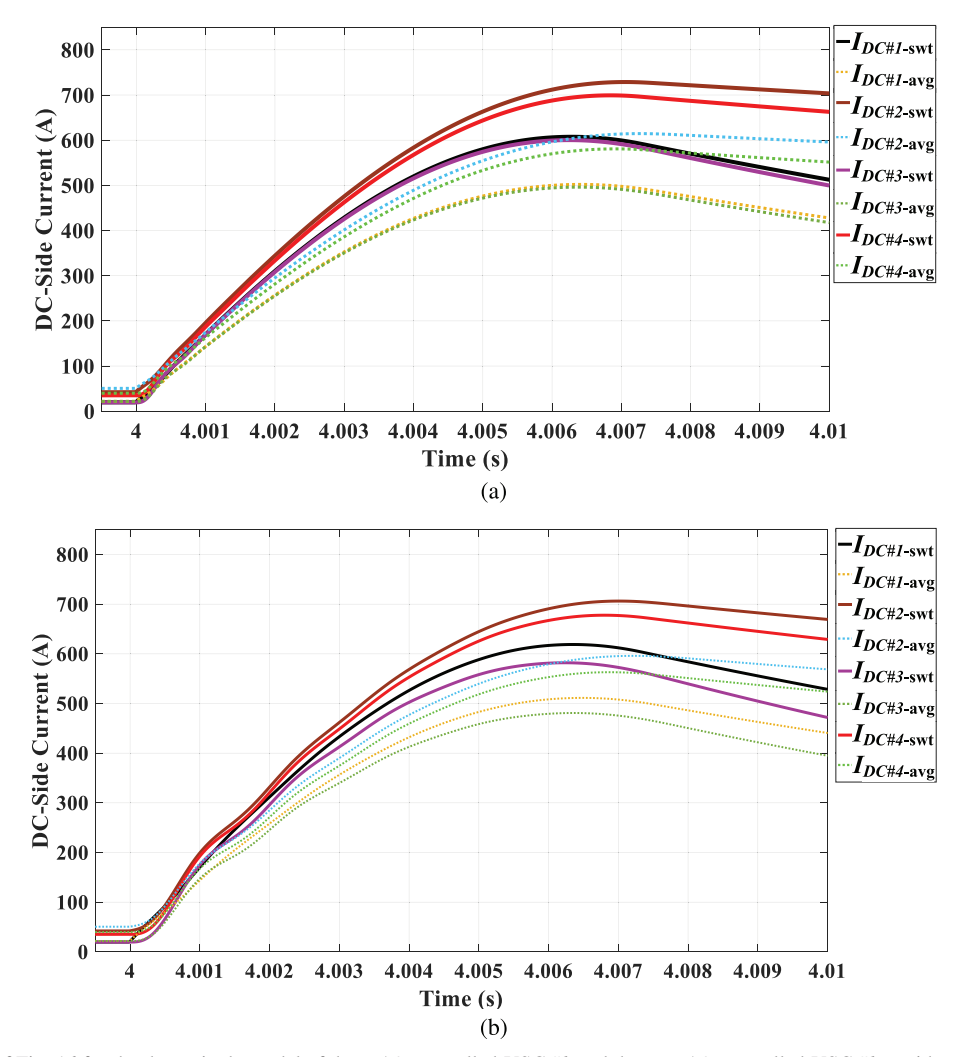


Fig. 18. Simulations of Fig. 16 for the dynamic dc model of the P/Q-controlled VSC #k and the V_{DC}/Q -controlled VSC #k—without considering $TF_{I_{AC}\#k}(s)$ and $K_{V_{DC}\#k}(s)/K_{I_{AC}\#k}(s)$ —subparts are not required to be shown here because the difference between the results of the switching models and those of the employed models is transparent and legible.

B. Previous Models—Which Are Not Considering Detailed Dynamics With Controllers

In order to demonstrate the effectiveness of the proposed models more clearly, the previous models that have not included the detailed dynamics with controllers are simulated and provided in the current subsection. For comparison of the models proposed in this article, all cases mentioned in Section III-A have been repeated, reproduced, and simulated for the conventionally proposed, old models. They have not included control dynamics, have ignored their detailed dynamics, and have only considered dc-side filters in the dc grid (see [10] and references therein).

Figs. 17 and 18 have shown the results when using the dynamic dc model of the P/Q-controlled VSC #k and the $V_{\rm DC}/Q$ -controlled VSC #k—without considering ${\rm TF}_{I_{\rm AC}\#k}(s)$ and $K_{V_{\rm DC}\#k}(s)/K_{I_{\rm AC}\#k}(s)$. Fig. 17 depicts the counterpart of Fig. 15, and Fig. 18 shows the counterpart of Fig. 16 for the abovementioned case.

When comparing Fig. 17 with Fig. 15 and Fig. 18 with Fig. 16, respectively, it will be apparent that the proposed detailed model is able to simulate the dc current

during dc faults much more accurately—and the results of the proposed models are tracking and following those of the switching models very well. The differences are caused by the "ignored" detailed dynamics made by controllers of $K_{V_{DC}\#k}(s)/K_{I_{AC}\#k}(s)$. Indeed, the close dynamics created by them will show their impacts when the circuit's dynamics get more nonlinear, thereby getting more dependent on operating points. This issue is getting worse when the grids to which VSCs are connected are weak (or very weak), thus having stronger closed-loop dynamics (made by controllers) influencing the time response dc variables.

IV. CONCLUSION

This article has proposed a DDDC model for grid-connected voltage-sourced converters. The model can be employed in dc-fault simulations in MMGs having MIACDC power architecture. This research has bridged the gap between controls and dynamic dc models of VSCs, which are being employed in the dc-fault simulation studies (applicable to the MMG protection). DDDC models of VSCs for their two principal operation modes, i.e., P/Q- and V_{DC}/Q -controlled ones, have been

proposed. The detailed VSC's dynamics of ac- and dc-side filters have been entirely taken into account. In this research, those dynamics have been derived by VSC's space-phasor representation, and after linearizing them, the relevant VSCs' controls have been used in creating the proposed models. Those controls have induced new dynamics that have been overlooked. Model validations have been done on a test rig consisting of a VSC as a prototype. Besides, the comparisons of time-domain simulations of the proposed models and those of the accurate switching models confirm the proposed models' validity. To this end, an MMG with MIACDC structure has been simulated in PSCAD/EMTDC software. The MMG has been simulated and run by PSCAD/EMTDC using both DDDC models and switching ones; simulations give the same results. Noticeably, in the end, comparative simulations have also been provided by using old models that did not consider controller dynamics. Analogizing the proposed DDDC models' results with conventionally adopted models ignoring controls and detailed dynamics has demonstrated that this research can have filled in gaps in the necessary models.

APPENDIX

The coefficients of a, b, e, A, B, and E in (10) are found in the following:

$$\begin{cases} a \triangleq -1.5L_{\text{f-DC\#k}}L_{\text{f-AC\#k}} \frac{P_{\text{PCC\#k0}}I_{\text{d-AC\#k0}}}{V_{\text{DC0\#k}}^2} \\ b \triangleq -L_{\text{f-DC\#k}} \frac{P_{\text{PCC\#k0}}}{V_{\text{DC0\#k}}^2} (3.0R_{\text{t-AC\#k}}I_{\text{d-AC\#k0}} \\ + 1.5L_{\text{f-AC\#k}}I_{\text{d-AC\#k0}} + 1.5V_{\text{d-PCC\#k0}}) \\ - 1.50L_{\text{f-AC\#k}}I_{\text{d-AC\#k0}} - 1.5V_{\text{d-PCC\#k0}} \\ e \triangleq -3.0R_{\text{t-AC\#k}}I_{\text{d-AC\#k0}} - 1.5V_{\text{d-PCC\#k0}}. \end{cases}$$

$$\begin{cases} A \triangleq L_{\text{f-DC\#k}}C_{\text{f-DC\#k}} \frac{P_{\text{PCC\#k0}}}{V_{\text{DC0\#k}}} \\ B \triangleq C_{\text{f-DC\#k}}V_{\text{DC0\#k}} - L_{\text{f-DC\#k}} \frac{P_{\text{PCC\#k0}}^2}{V_{\text{DC0\#k}}^3} \\ E \triangleq \frac{2V_{\text{DC0\#k}}}{R_{\text{P\#k}}}. \end{cases}$$
(A.2)

ACKNOWLEDGMENT

The authors would like to thank SEMIKRON Company (https://www.semikron.com/), Verivolt Company (https://www.verivolt.com), and dSPACE GmbH Company (https://www.dspace.com/en/inc/home.cfm) for kindly providing Georgia Southern University with financial support in part.

REFERENCES

- [1] US Department of Energy. (Nov. 2014). (The War of the Currents: AC vs. DC Power). [Online]. Available: http://energy.gov/articles/war-currents-ac-vs-dc-power
- [2] M. Davari, W. Gao, and F. Blaabjerg, "Analysing dynamics and synthesising a robust vector control for the DC-voltage power port based on the modular multilevel converter in multi-infeed AC/DC smart grids," *IET Smart Grid*, vol. 2, no. 4, pp. 645–658, Dec. 2019.
- [3] IEEE Application Guide for IEEE Std. 1547(TM), IEEE Standard For Interconnecting Distributed Resources With Electric Power Systems, Standard 1547.2-2008, Apr. 2009.
- [4] Standard for Inverters, Converters, Controllers and Interconnection System Equipment for Use With Distributed Energy Resources, Standard UL1741, Jan. 2010.

- [5] Rule 21 Interconnection, California Public Utility Commission, San Francisco, CA, USA, Jul. 2017.
- [6] R. Das, V. Madani, and A. P. S. Meliopoulos, "Leveraging smart grid technology and using microgrid as a vehicle to benefit DER integration," in *Proc. IEEE Power Energy Soc. Innov. Smart Grid Technol. Conf.* (ISGT), Apr. 2017, pp. 1–5.
- [7] J. Shiles et al., "Microgrid protection: An overview of protection strategies in north American microgrid projects," in Proc. IEEE Power Energy Soc. Gen. Meeting, Jul. 2017, pp. 1–5.
- [8] I. U. Nutkani et al., "Autonomous power management for interlinked AC-DC microgrids," CSEE J. Power Energy Syst., vol. 4, no. 1, pp. 11–18, Mar. 2018.
- [9] H. S. Samkari and B. K. Johnson, "Multi-agent protection scheme for resilient microgrid systems with aggregated electronically coupled distributed energy resources," in *Proc. 44th Annu. Conf. Ind. Electron.* Soc., Oct. 2018, pp. 752–757.
- [10] L. Xu, "Modeling, analysis and control of voltage-source converter in microgrids and HVDC," Ph.D. dissertation, Dept. Elect. Eng., Univ. South Florida, Tampa, FL, USA, Nov. 2013. [Online]. Available: https://scholarcommons.usf.edu/etd/4967/
- [11] A. Hooshyar and R. Iravani, "Microgrid protection," Proc. IEEE, vol. 105, no. 7, pp. 1332–1353, Jul. 2017.
- [12] A. Hooshyar and R. Iravani, "A new directional element for microgrid protection," *IEEE Trans. Smart Grid*, vol. 9, no. 6, pp. 6862–6876, Nov. 2018.
- [13] H. Muda and P. Jena, "Superimposed adaptive sequence current based microgrid protection: A new technique," *IEEE Trans. Power Del.*, vol. 32, no. 2, pp. 757–767, Apr. 2017.
- [14] R. Mohanty and A. K. Pradhan, "A superimposed current based unit protection scheme for DC microgrid," *IEEE Trans. Smart Grid*, vol. 9, no. 4, pp. 3917–3919, Jul. 2018.
- [15] V. Telukunta et al., "Protection challenges under bulk penetration of renewable energy resources in power systems: A review," CSEE J. Power Energy Syst., vol. 3, no. 4, pp. 365–379, Dec. 2017.
- [16] S. F. Zarei and M. Parniani, "A comprehensive digital protection scheme for low-voltage microgrids with inverter-based and conventional distributed generations," *IEEE Trans. Power Del.*, vol. 32, no. 1, pp. 441–452, Feb. 2017.
- [17] W.-M. Guo, L.-H. Mu, and X. Zhang, "Fault models of inverter-interfaced distributed generators within a low-voltage microgrid," *IEEE Trans. Power Del.*, vol. 32, no. 1, pp. 453–461, Feb. 2017.
- [18] M. A. Haj-ahmed and M. S. Illindala, "Investigation of protection schemes for flexible distribution of energy and storage resources in an industrial microgrid," *IEEE Trans. Ind. Appl.*, vol. 51, no. 3, pp. 2071–2080, May 2015.
- [19] K. O. Oureilidis and C. S. Demoulias, "A fault clearing method in converter-dominated microgrids with conventional protection means," *IEEE Trans. Power Electron.*, vol. 31, no. 6, pp. 4628–4640, Jun. 2016.
- [20] H. Laaksonen, D. Ishchenko, and A. Oudalov, "Adaptive protection and microgrid control design for hailuoto island," *IEEE Trans. Smart Grid*, vol. 5, no. 3, pp. 1486–1493, May 2014.
- [21] A. Aghazadeh, M. Davari, H. Nafisi, and F. Blaabjerg, "Grid integration of a dual two-level voltage-source inverter considering grid impedance and phase-locked loop," *IEEE J. Emerg. Sel. Topics Power Electron.*, early access, Nov. 14, 2019, doi: 10.1109/JESTPE.2019.2953522.
- [22] M. Davari and Y. A.-R. I. Mohamed, "Robust vector control of a very weak-grid-connected voltage-source converter considering the phaselocked loop dynamics," *IEEE Trans. Power Electron.*, vol. 32, no. 2, pp. 977–994, 2017.
- [23] M. Davari, W. Gao, and F. Blaabjerg, "A fault-tolerant, passivity-based controller enhanced by the equilibrium-to-equilibrium maneuver capability for the DC-voltage power port vsc in multi-infeed AC/DC modernized grids," *IEEE J. Emerg. Sel. Topics Power Electron.*, vol. 8, no. 3, pp. 2484–2507, Sep. 2020. [Online]. Available: https://ieeexplore.ieee.org/abstract/document/8718605/
- [24] M. Davari and Y. A.-R.-I. Mohamed, "Dynamics and robust control of a grid-connected VSC in multiterminal DC grids considering the instantaneous power of DC- and AC-side filters and DC grid uncertainty," *IEEE Trans. Power Electron.*, vol. 31, no. 3, pp. 1942–1958, Mar. 2016.
- [25] M. Davari, M. Aghababa, F. Blaabjerg, and M. Saif, "A modular adaptive robust nonlinear control for resilient integration of VSIs into emerging modernized microgrids," *IEEE J. Emerg. Sel. Topics Power Electron.*, early access, Mar. 30, 2020, doi: 10.1109/JESTPE.2020.2984231.
- [26] M. P. Kazmierkowski and L. Malesani, "Current control techniques for three-phase voltage-source PWM converters: A survey," *IEEE Trans. Ind. Electron.*, vol. 45, no. 5, pp. 691–703, Oct. 1998.

- [27] A. Yazdani and R. Iravani, Voltage-Sourced Converters in Power Systems: Modeling, Control, and Applications. Hoboken, NJ, USA: Wiley, 2010, pp. 204–244, ch. 8.
- [28] B. Bahrani, S. Kenzelmann, and A. Rufer, "Multivariable-PI-based dq current control of voltage source converters with superior axis decoupling capability," *IEEE Trans. Ind. Electron.*, vol. 58, no. 7, pp. 3016–3026, Jul. 2011.
- [29] A. Egea-Alvarez, S. Fekriasl, F. Hassan, and O. Gomis-Bellmunt, "Advanced vector control for voltage source converters connected to weak grids," *IEEE Trans. Power Syst.*, vol. 30, no. 6, pp. 3072–3081, Nov. 2015.
- [30] N. Panten, N. Hoffmann, and F. W. Fuchs, "Finite control set model predictive current control for grid-connected voltage-source converters with LCL filters: A study based on different state feedbacks," *IEEE Trans. Power Electron.*, vol. 31, no. 7, pp. 5189–5200, Jul. 2016.
- [31] D. Zhou, Y. Song, and F. Blaabjerg, Control of Power Electronic Converters and Systems: Volume 1. New York, NY, USA: Academic, 2018, pp. 117–151.
- [32] J. B. Nørgaard, M. K. Graungaard, T. Dragičević, and F. Blaabjerg, "Current control of LCL-filtered grid-connected vsc using model predictive control with inherent damping," in *Proc. 20th Eur. Conf. Power Electron. Appl.*, Nov. 2018, pp. 1–11.
- [33] A. Yazdani and R. Iravani, Voltage-Sourced Converters in Power Systems: Modeling, Control, and Applications. Hoboken, NJ, USA: Wiley, 2010, pp. 1–20.
- [34] A. Yazdani and R. Iravani, Voltage-Sourced Converters in Power Systems: Modeling, Control, and Applications. Hoboken, NJ, USA: Wiley, 2010, pp. 38–47.
- [35] O. S. Senturk, L. Helle, S. Munk-Nielsen, P. Rodriguez, and R. Teodorescu, "Converter structure-based power loss and static thermal modeling of the press-pack IGBT three-level ANPC VSC applied to multi-MW wind turbines," *IEEE Trans. Ind. Appl.*, vol. 47, no. 6, pp. 2505–2515, Nov. 2011.
- [36] C. A. Desoer and E. S. Kuh, Basic Circuit Theory. New York, NY, USA: McGraw-Hill, 1969, pp. 653–699, ch. 16.



Masoud Davari (Senior Member, IEEE) was born in Isfahan, Iran, in September 1985. He received the B.Sc. degree (Hons.) in electrical engineering power from the Isfahan University of Technology, Isfahan, in September 2007, the M.Sc. degree (Hons.) in electrical engineering-power from the Amirkabir University of Technology (Tehran Polytechnic), Tehran, Iran, in January 2010, and the Ph.D. degree in electrical engineering–energy systems from the University of Alberta, Edmonton, AB, Canada, in January 2016.

He was with the Iran's Grid Secure Operation Research Center, Tehran, and the Iran's Electric Power Research Institute (EPRI), Tehran, from January 2010 to December 2011. From April 2015 to June 2017, he has collaborated with Quanta-Technology Company, Markham, ON, Canada, in the field of the dynamic interaction of renewable energy systems with smart grids, as well as control, protection, and automation of microgrids, as a Senior Research and Development Specialist and a Senior Consultant. In July 2017, he joined the Department of Electrical and Computer Engineering, Allen E. Paulson College of Engineering and Computing, Georgia Southern University, Statesboro, GA, USA, as a tenure-track Assistant Professor. He has developed and implemented several experimental test rigs for both research universities and the industry. He has also authored several IEEE TRANSACTIONS and journals. His research interests include the dynamics, controls, and protections of different types of power electronic converters that are utilized in the hybrid ac/dc smart grids and hardware-in-the-loop (HIL) testing of modernized power systems.

Dr. Davari has been serving as an Active Member and a Chapter Lead (for Chapter 3) of the IEEE WG P2004, a newly established IEEE working group on the HIL simulation for the IEEE Standards Association, since June 2017. He is also an Invited Member of the Golden Key International Honour Society. He was awarded the Allen E. Paulson College of Engineering and Computing (CEC) Faculty Award for Scholarly Activity in the Allen E. Paulson CEC, Georgia Southern University, from 2019 to 2020, and the Best Reviewer of the IEEE TRANSACTIONS ON POWER SYSTEMS in 2018. He has served as the Chair of the Literature Review Subgroup of DC@home Standards for the IEEE Standards Association from April 2014 to October 2015. He is also an Invited Reviewer of several of the IEEE TRANSACTIONS and journals, IET journals, *Energies* journal, and various IEEE conferences, as well as an invited speaker at different universities and in diverse societies.



Amir Aghazadeh was born in Tehran, Iran. He received the B.S. degree in electrical engineering from the Sadra Institute of Higher Education, Tehran, in 2010, and the M.S. degree in electrical engineering from the Amirkabir University of Technology (AUT), Tehran, in 2014. He is currently pursuing the Ph.D. degree in electrical engineering with the School of Electronic and Electrical Engineering, University of Leeds, Leeds, U.K.

In 2013, he has established the Golden Group (G2) at AUT working on emerging and selected topics

in power electronics. His research interests include power electronics, its application in power systems, and high-speed railway power supply system protection and controls.



Weinan Gao (Member, IEEE) received the B.Sc. degree in automation and the M.Sc. degree in control theory and control engineering from Northeastern University, Shenyang, China, in 2011 and 2013, respectively, and the Ph.D. degree in electrical engineering from New York University, New York, NY, USA, in 2017.

He was an Assistant Professor of electrical and computer engineering with Georgia Southern University, Statesboro, GA, USA, from 2017 to 2020, and a Visiting Professor with the Mitsubishi Electric

Research Laboratories, Cambridge, MA, USA, in 2018. He is currently an Assistant Professor of mechanical and civil engineering with the Florida Institute of Technology, Melbourne, FL, USA. His research interests include reinforcement learning, adaptive dynamic programming (ADP), optimal control, cooperative adaptive cruise control (CACC), intelligent transportation systems, sampled-data control systems, and output regulation theory.

Dr. Gao is also a member of the Editorial Board of *Neural Computing and Applications*. He was a recipient of the Best Paper Award at the IEEE International Conference on Real-Time Computing and Robotics (RCAR) in 2018 and the David Goodman Research Award from the Department of Electrical and Computer Engineering, New York University, in 2019. He is also an Associate Editor of the IEEE/CAA JOURNAL OF AUTOMATICA SINICA and *Neurocomputing*.



Frede Blaabjerg (Fellow, IEEE) received the Ph.D. degree in electrical engineering from Aalborg University, Aalborg, Denmark, in 1995, the Honoris Causa degree from Universitatea Politehnica Timisoara (UPT), Timisoara, Romania, in 2017, and the Honoris Causa degree from the Tallinn University of Technology (TTU), Tallinn, Estonia, in 2018.

He was with ABB-Scandia, Randers, Denmark, from 1987 to 1988. He became an Assistant Professor at the Department of Energy Technology, Aalborg University, in 1992, where he became an

Associate Professor in 1996 and a Full Professor of power electronics and drives in 1998 and has been a Villum Investigator since 2017. He has authored or coauthored more than 600 journal articles in different fields of power electronics and its applications, coauthored four monographs, and edited ten books in power electronics and its applications. His current research interests include power electronics and its applications, such as in wind turbines, photovoltaic systems, reliability, harmonics, and adjustable speed drives.

Dr. Blaabjerg received the 31 IEEE Prize Paper Awards, the IEEE PELS Distinguished Service Award in 2009, the EPE-PEMC Council Award in 2010, the IEEE William E. Newell Power Electronics Award in 2014, and the Villum Kann Rasmussen Research Award in 2014. He was a recipient of the Global Energy Award for a significant contribution to the development of technologies that provide new energy development opportunities in 2019. He was a recipient of the IEEE Edison Medal in 2020. He was nominated by Thomson Reuters to be included in the 250 most-cited researchers in engineering in the world from 2014 to 2018. He is also the President of the IEEE Power Electronics Society for the term 2019–2020 and the Vice President of the Danish Academy of Technical Sciences. He was the Editor-in-Chief of the IEEE TRANSACTIONS ON POWER ELECTRONICS from 2006 to 2012. He was a Distinguished Lecturer of the IEEE Power Electronics Society from 2005 to 2007 and the IEEE Industry Applications Society from 2010 to 2011 and 2017 to 2018.